The Morphology of Martian Pyroclastic Ramparts and Their Use in Determining Vent-Proximal Eruption Dynamics

B. Pieterek[1,2], T. J. Jones[3] and L. Wilson[3]

[1]Polish Geological Institute – National Research Institute, Warsaw, Poland

[2]Geohazard Research Unit, Institute of Geology, Adam Mickiewicz University in Poznań

[3]Lancaster Environment Centre, Lancaster University, Lancaster LA1 4YQ, UK

Corresponding author: Bartosz Pieterek (bpieterek94@gmail.com)

Key Points:

- Investigation of vent-proximal volcanic products allowed the eruption dynamics of a fissure system to be reconstructed
- The spatial distribution of spatter rampart deposits along the fissure vent is heterogeneous and related to dynamic eruption processes
- Amazonian-aged basaltic volcanism involves both effusive activity and low-intensity explosive eruptions

Abstract

High-resolution investigations of Late Amazonian volcanic landforms provide previously unrevealed insights into the dynamics of Martian volcanic eruptions. On Earth, the formation of vent-proximal accumulations of spatter deposits is attributed to low-intensity lava fountaining episodes representing eruptions on the very edge of explosive activity. Martian spatter deposits form small-scale volcanic landforms that are rarely reported, and thus the dynamics of Martian mafic explosive eruptions is still not fully constrained. We conducted high-resolution Context Camera-based mapping coupled with a stereo-pair-generated digital elevation model to reconstruct the eruptive history of a fissure system and its associated products south of Ascraeus Mons, Mars. The studied volcanic fissure clearly demonstrates both explosive and effusive deposits and, in addition, is spatially associated with a lava channel. For the first time, these observations allowed us to conduct a comparative analysis of vent-proximal volcanic products and reconstruct the late-stage eruption dynamics of a fissure system. We found that the spatial distribution of the pyroclastic (spatter) rampart along the fissure vent is heterogeneous and generated by dynamic eruption processes. Moreover, the lava channel fed from the fissure vent shows evidence of successive lava overspills whose emplacement was topographically controlled. These observations suggest that, in contrast to the general inference that Amazonian-age volcanism mainly involves effusive eruptions, explosive-origin landforms might have been overlooked. Therefore, we argue that high-resolution mapping of pyroclastic deposits may provide critical insights into understanding the dynamic nature of Martian fissure eruptions and explosive-associated volatile release during the last stages of eruptions.

Plain Language Summary

Although it is widely accepted that Martian volcanism has mainly involved widespread lava effusion, the increased acquisition of high-resolution satellite images is challenging this viewpoint and providing new insights into the dynamics of volcanic eruptions. A better understanding of the small-scale volcanic landforms on Mars increases our understanding of volcanism in general. As Tharsis, the largest volcanic province on Mars, hosts hundreds of volcanic fissure vents and associated landforms, it constitutes the best natural laboratory for the investigation of volcanic products deposited near to the vent. Here, we conducted high-resolution mapping of the near-vent accumulations of fragmented lava, called spatter deposits, which

allows us to reconstruct the eruption dynamics during the waning stages. Our observations suggest that the spatter deposits are attributed to low-intensity lava fountaining of explosive origin, whereas the adjacent lava flow channels are rimmed by successive lava overspills. These observations suggest that Martian fissure systems experienced two eruptive styles simultaneously. However, to date, on Mars, the explosive-origin landforms associated with fissure vents have been overlooked. Overall, our study indicates the importance of conducting detailed studies of small-scale volcanic landforms that record complex and previously undiscovered dynamics of Martian volcanic systems.

Keywords: spatter deposits, fragmentation, volcanism, explosive eruptions, rheomorphic

1 Introduction

Throughout the entire history of the planet, the interior structure and surface volcanic features of Mars have been controlled by magmatic processes, especially focused within the volcanic provinces of Tharsis and Elysium (Mouginis-Mark et al., 2022; Werner, 2009; Zimbelman et al., 2015). For example, as revealed by orbital observations, the Tharsis volcanic province constitutes ~25% of the Martian surface, and is dominated by the Amazonian-age plains-style effusive volcanism evidenced by abundant dyke-fed fissure vents and low-shield volcanoes (Hauber et al., 2009, 2011; Pieterek et al., 2022b; Richardson et al., 2021). Nevertheless, in some regions on Mars, there is evidence suggesting that eruptions of more differentiated magma compositions were common in the Amazonian and resulted in the formation of local-scale explosive-origin volcanic fields and landforms (Brož et al., 2017; Brož & Hauber, 2012; Horvath et al., 2021; Pieterek et al., 2022a; 2024; Wilson et al., 2009). An Amazonian age for these features contradicts the inference of a key change of the eruptive style from explosive to effusive at the transition between the Noachian and Hesperian, at approximately 3.5 Ga (Robbins et al., 2011). Detailed observations of volcanic products and landforms at high spatial resolution using remotely sensed data provide a means to shed new light on our understanding of the volcanic history of Mars (Peters et al., 2021; Pieterek et al., 2024; Pieterek & Jones, 2023). Here, we focus on reconstructing the eruptive history and associated products of a fissure system south of Ascraeus Mons, Mars, which clearly exhibits deposits formed by both explosive and effusive volcanic eruptions.

On Earth, steep-sided, vent-proximal accumulations of agglutinated pyroclastic material (i.e., spatter) are termed spatter ramparts if laterally extensive, or spatter mounds if isolated. These are typically associated with low intensity lava fountaining episodes of mafic magma (Houghton & Gonnermann, 2008; Parcheta et al., 2012, 2015; Taddeucci et al., 2015). They represent eruptions on the cusp of explosive activity, fragmenting the erupted magma by predominantly ductile processes (Jones et al., 2019; Jones et al., 2022b). However, to date on Mars, such products of (weakly) explosive volcanic eruptions have been rarely described (Hauber et al., 2009; Mouginis-Mark & Christensen, 2005; Wilson et al., 2009), and therefore, the understanding of explosive basaltic eruptions is still not fully constrained. There is evidence that individual mafic fissure systems on Mars can experience varying eruptive styles, yielding different volcanic products, landforms and morphologies (Hauber et al., 2009; Pieterek & Jones, 2023; Wilson & Head, 1994). The presence of spatter ramparts along vent-proximal portions of fissure vents is mainly attributed to magmas, perhaps volatile-rich, that erupt explosively (Mouginis-Mark & Christensen, 2005; Wilson et al., 2009).

When preserved, volcanic fissures and their associated vent-proximal products (e.g., spatter mounds, spatter ramparts) can directly inform on the eruption styles, dynamics, and their temporal evolution (Wilson et al., 2009). Despite this, relatively few studies have documented vent-proximal pyroclastic deposits associated with Martian volcanoes (Mouginis-Mark & Christensen, 2005; Wilson et al., 2009). This knowledge gap can be attributed to multiple factors: (i) spatter ramparts and mounds are relatively small (<1 km in size) constructs. Thus, for identification, high resolution topographic data are required. Such data have only recently been available on the local scale by applying the Context Camera (CTX)-based or even more precise High Resolution Imaging Science Experiment (HiRISE)-based digital elevation models (DEMs) (Brož et al., 2015; Pieterek & Jones, 2023; Vörös & Székely, 2022). (ii) The preservation potential of vent-proximal deposits is very poor. They are often buried by later eruptive products (Brož & Hauber, 2011; Pieterek & Jones, 2023; Vaucher et al., 2009), can behave rheomorphically and flow away from the vent (Sumner, 1998), and are susceptible to erosion both during and after the eruption (Apuani et al., 2005; Le Moigne et al., 2022; Romero et al., 2022; Sutton et al., 2024). (iii) Lastly, there is a range of linear features on Mars, including fractures, grabens, fissures, lava channels, lava tubes, and pit chains. Therefore, distinguishing fissure-associated pyroclastic ramparts from other linear constructs, such as lava channels with elevated rims, can be difficult.

In this study, we used CTX-based topographic data to perform a detailed reconstruction of the vent-proximal depositional units associated with a fissure eruption. By doing this we provide fundamental insights into the eruption dynamics and the fissure evolution. Moreover, our mapping approach yields robust quantitative geometric properties (e.g., depth, width, height) of fissure vents and their pyroclastic ramparts. These data can support the correct identification and mapping of pyroclastic ramparts from other linear structures of various origins (i.e., volcanic and tectonic) present on the Martian surface.

2 Geological setting

The largest volcanic province on Mars, Tharsis, constitutes nearly a quarter of the Martian surface and hosts three volcanoes aligned in the SW-NE direction, namely, Arsia Mons, Pavonis Mons, and Ascraeus Mons (Tharsis Montes; Fig. 1). Their southeastern flanks host the highest concentrations of distributed volcanic landforms found on the Martian surface (Bleacher et al., 2009; Hauber et al., 2011; Pieterek et al., 2022b; Richardson et al., 2021); Fig. 1a). These volcanic landforms mainly comprise low shield volcanoes, fissure vents, or circular vents with associated lava flows, and a relatively wide variety of other volcanic units that cannot be directly linked to their eruptive centers because the younger deposits partially cover older landforms (Bleacher et al., 2007; Hauber et al., 2009). Nevertheless, regional spatiotemporal reconstruction shows that the Late Amazonian distributed volcanism located southeast of the Tharsis Montes volcanoes might be either related to the adjacent major volcanoes' plumbing systems (Pieterek et al., 2022b) or an extended underplating zone emplaced at the crust-mantle boundary beneath the Martian lithosphere southeast of Tharsis Montes (Richardson et al., 2021). The age determinations of the volcanic edifices and lava flows to the south of Pavonis Mons and Ascraeus Mons reveal young (from 50 to 173 Ma) emplacement ages (Hauber et al., 2011; Pieterek et al., 2022b), and therefore these areas are considered to constitute the best field laboratory for investigating volcanic processes and better understanding Martian eruptions (Pieterek & Jones, 2023; Wilson et al., 2009). Moreover, the relatively young ages (< 100 Ma) of the latest volcanic activity (Hauber et al., 2011; Pieterek et al., 2022b) and low erosion rates on

Mars (Carr & Head III, 2010; Golombek et al., 2006) cause these landforms to maintain good preservation states allowing us to conduct high-resolution observations.

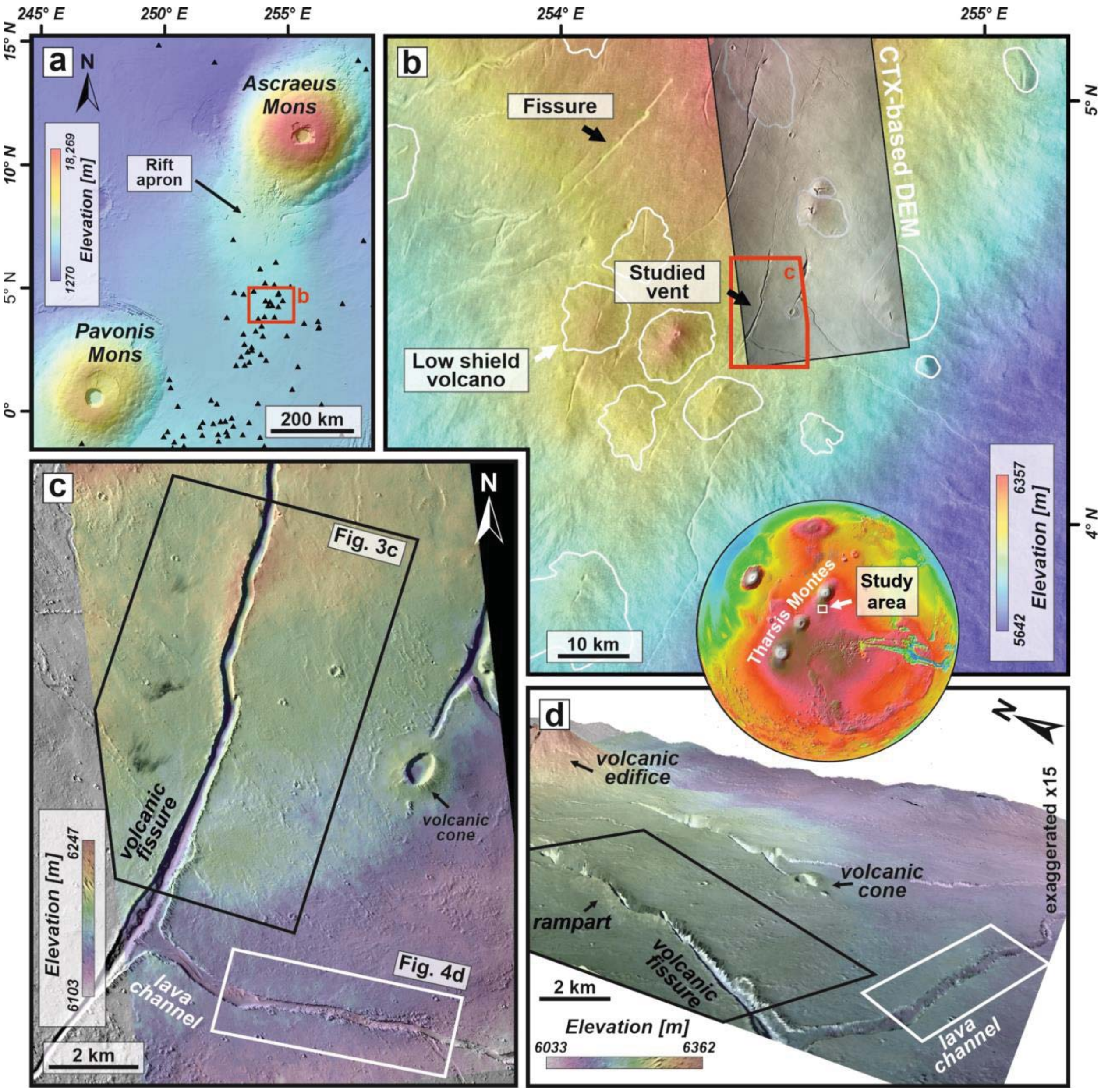

Fig. 1 Geological context of the fissure system, associated pyroclastic/spatter ramparts and lava flows. The middle, circular inset shows the topographic map of Mars with the white rectangle indicating the location of the study area. **(a)** An overview map of two major volcanoes located within the Tharsis Montes region. Previously, Pieterek et al. (2022b) mapped distributed volcanoes marked by black triangles. **(b)** Topographic map of the southern region of Ascraeus Mons with outlines of the low shield volcanoes (white lines) and linear features interpreted as volcanic fissures (black arrows). Note that the entire region hosts numerous linear features whose origin might be debatable. In both panels, the base map is a blend of digital elevation model (200 m/px; Fergason et al., 2018) derived from the Mars Orbiter

Laser Altimeter (MOLA) and High-Resolution Stereo Camera (HRSC) and a global daytime infrared mosaic of the Thermal Emission Imaging System (THEMIS) (100 m/px; Edwards et al., 2011). **(c)** Topographic map of the study area showing the investigated fissure vent and lava channel. The Context Camera (CTX) image (B17_016463_1840, centered at 4.07°N and 254.44°E) is overlaid by the produced CTX-based DEM (for details see Data and Methods). **(d)** The corresponding 3D view of the study area showing the spatial relationship between various volcanic landforms with a special focus on investigated vent-proximal deposits (rampart) and lava channel. The image is produced using CTX-based DEM exaggerated 15 times.

Tharsis Montes volcanoes are characterized by rift apron flows (Fig. 1a) which form scallop-shaped rises abutting the north/northeastern and south/southwestern flanks of each large shield volcano (Bleacher et al., 2007). On top of these widespread flows, emplacement of the small-scale volcanic landforms (e.g., low shield volcanoes, volcanic fissure vents) has led to the formation of volcanic clusters (Fig. 1b). Richardson et al. (2021) proposed that these rift apron deposits and landforms might be supplied by a common magmatic source region. This hypothesis is supported by the common ages (Giacomini et al., 2009) and superposition relationships (Bleacher et al., 2007) of the rift apron lavas and the distributed low-shield cones. Additionally, the summit vent alignments on the rift aprons of each Tharsis Montes volcano show consistent orientations parallel to the regional NW-SE direction and are radially oriented to the adjacent major volcano (Pieterek et al., 2022b; Richardson et al., 2021).

The fissure vent system studied here is situated to the south of Ascraeus Mons, on top of the associated rift apron, and so the regional topography decreases towards the southwest (Fig. 1b). This topography is expressed by the predominant NE-SW direction of the linear structures which are consistent with radially-oriented dykes originating from Ascraeus Mons (Pieterek et al., 2022b). Our fissure system is accompanied by a cluster of distributed volcanoes and other linear features including lava channels and lava tubes. Among the volcanic fissures (Fig. 1b), the investigated vent shows clear geological association with a lava channel (Fig. 1c-d) allowing us to conduct precise determinations of morphological parameters and compare these two different linear structures (volcanic fissure vs. lava channel) without any doubts about their origin.

3 Data and Methods

To identify and map both the volcanic fissure and lava channel deposits, we used a global daytime infrared mosaic of the Thermal Emission Imaging System (THEMIS; Edwards et al., 2011) with a spatial resolution of 100 m/px for selecting regions of interest. The Context Camera images (CTX) from the Mars Reconnaissance Orbiter (MRO; Malin et al., 2007) was then used for mapping. The ground sampling distance of ~5 m/px for the CTX images provided sufficient spatial resolution to conduct detailed mapping and allowed us to identify volcanic landforms and associated flow-like features that occur on both sides of the fissure and channel. During our initial mapping campaign of the volcanic regions, the THEMIS images showed brighter regions on one side of the volcanic vent suggesting a steep slope comprising rocky material with warmer nighttime temperatures, and thus the highest thermal inertia values relative to the surrounding areas (Edwards et al., 2011). Due to the low resolution of THEMIS and the small size of considered landforms, such observations must be supplemented by high-resolution CTX-based DEMs. To conduct a detailed topographic analysis of the regions of interest, we used DEMs derived from CTX stereo-pair images. The DEMs were produced using the data processing information system MarsSI (Mars System of Information) designed to process Martian orbital data (Quantin-Nataf et al., 2018). The CTX images that have been used to produce our DEM were P02_001774_1848, centered at 4.86°N, 254.60°E, and B01_009949_1844, centered at 4.46°N, 254.62°E. The CTX-based DEM has a scale of ~12 m per pixel and a vertical resolution of ~4 m allowing us to (i) conduct precise topographic measurements; (ii) determine the spatial extent of ramparts and (iii) determine the stratigraphic relationship between erupted materials, to provide relative age constraints and build an eruptive sequence. However, CTX-based DEMs are not free from vertical errors on elevations. In this study, we calculated the root-mean-square deviation of two overlapping CTX stereo-pairs using an additional CTX-based DEM (B01_009949_1844 centered at 4.46°N, 254.62°E, and F02_036427_1847, centered at 4.80°N, 254.61°E). We obtained a root-mean-square deviation value of 9.0 m which is consistent with literature data (e.g., Volat et al., 2022).

The morphology of the regions of interest was quantified using CTX images, supported by the corresponding elevation data (DEM). We used these to construct topographic cross-sections (Fig. 2) of vent-proximal deposits adjacent to the fissure vent and of lava channel-associated deposits. Using these cross-sections, we determined the spatial extent of the erupted material and mapped the outlines of distinguishable volcanic eruptive units (e.g., Fig. 2a). To conduct a systematic analysis of morphometric parameters, for both the volcanic fissure vent and lava channel, we firstly drew a midplane line always located at the center of the linear feature (i.e., the distance between the feature rim and the midplane is the same on both sides). We also drew parallel profile bounding lines along the strike of the investigated volcanic features (Fig. S1). These bounding lines extended 2.5 km and 1 km from the fissure and lava channel midplanes, respectively, and were drawn perfectly parallel. Along these bounding lines, every 200 meters, we generated points that constituted the start and end of the profile lines (Fig. S1) that were used for cross-section production. These profile lines are not always perfectly perpendicular (i.e., at 90°) to the midplane because we wanted to cover the mapped area evenly with thickness measurements. Instead, they deviated between 65° to 115°, at the most curved part of the fissure. Using the CTX-based DEM, we produced topographic cross-sections along the profile lines that had lengths of 5 and 2 kilometers for the fissure and lava channel, respectively (Fig. S1). The different profile lengths simply reflect the differences in spatial extent of the eruptive products. Based on the cross-sections produced, we determined several parameters to quantitatively characterize the morphology of the features. As the investigated features are not symmetrical, we measured all parameters on both sides of the midplane (Fig. 2). The geomorphic parameters we measured include the depth (D) and width (W) of both fissure and channel as well as thickness (T) and lateral extend (E) of the associated deposits (subscript depending on the feature, F for fissure and C for channel). The depth parameter is defined as the vertical distance between the highest elevation point of the vent-proximal deposits and the lowest elevation of the midplane, whereas the width is the horizontal distance from the midplane to the highest point of the studied deposits (Fig. 2). A graphical visualization of the morphological parameters is presented in Figure 2. By having measurements from both sides of the studied features, we calculated average values of selected parameters that are used in Figure 7.

Detailed geological mapping and cross-sections allowed us to determine the spatial extent defined as the horizontal distance from midplane to the furthest extent of the erupted material together with its thickness which was measured every 50 meters along the profile lines (parameter x in Fig. 2). Using the topographical profiles and our volcanic mapping, we determined a detectable break in the slope which constituted the furthest extent of the deposits. Assuming a relatively flat slope of the surrounding terrains (<0.4°; Fig. 1d), the elevation of this point was used as a base for our thickness measurements (Fig. 2). This approximation may slightly overestimate the obtained thickness results, especially at vent-proximal regions (see Section 5.1).

Our systematic thickness measurements at high-resolution were used to generate a thickness map of the pyroclastic/spatter ramparts and the lava channel deposits. The thickness maps were produced using the natural neighbor interpolation technique which is a spatial interpolation developed by Sibson (1981) that uses the average weight of the surrounding area. In this study, we also used inverse distance weighted (IDW) and Kriging techniques for the thickness map production; however, the maps obtained did not show any meaningful differences between one another (Fig. S2). All these interpolation techniques are available in the interpolation toolbox in the spatial analysis package for ArcGIS software. All image and data analysis associated with mapping was conducted using ArcGIS software version ArcMap 10.5 and our 3D visualizations were produced in ArcScene 10.5. The shapefiles containing the outlines of geological units and data pertaining to the thickness measurements of the spatter deposits are available in the Zenodo repository (Pieterek & Jones, 2024).

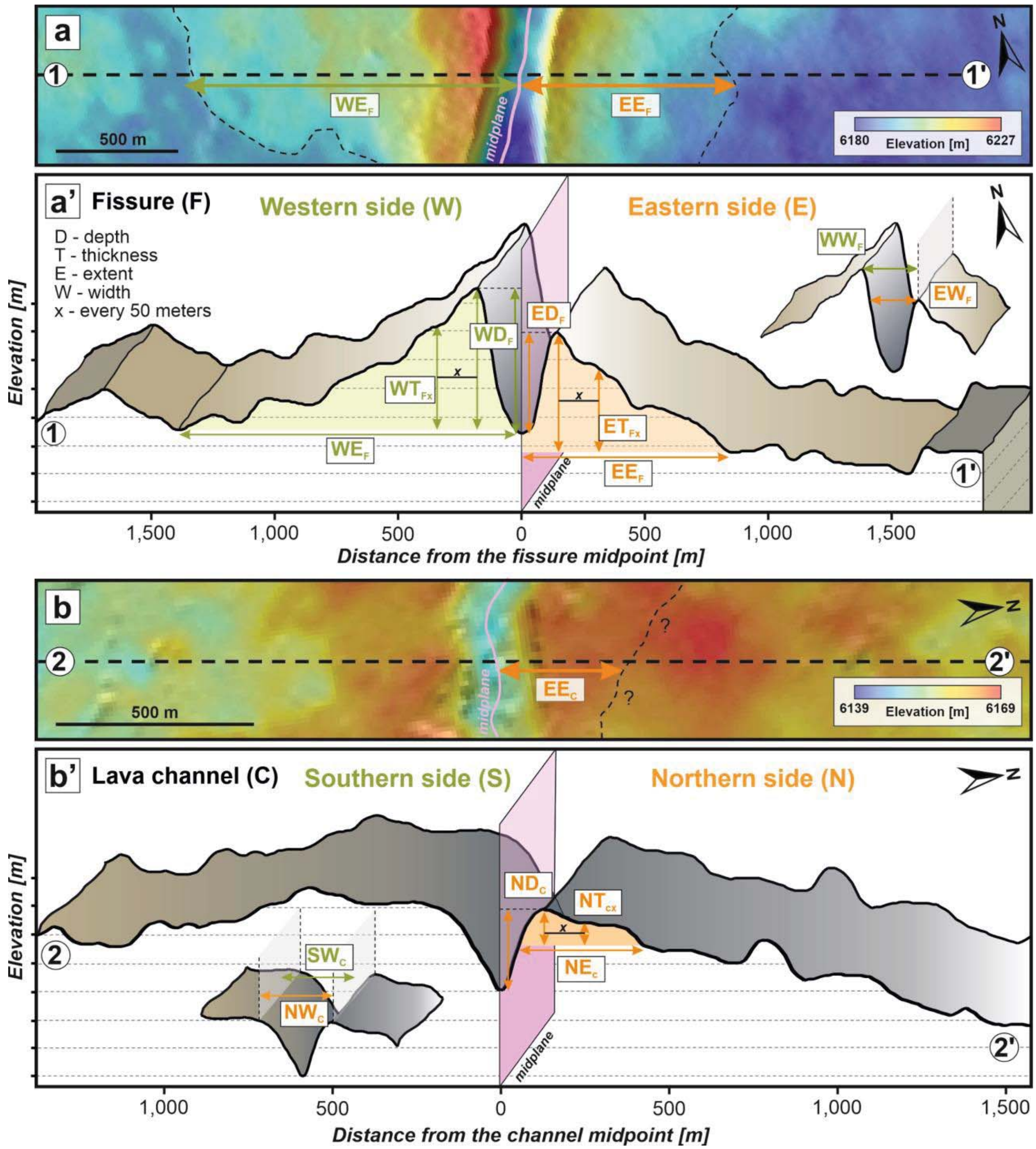

Fig. 2 Research methodology applied to characterize Martian volcanic fissures and lava channels. Topographic maps of **(a)** the volcanic fissure with associated pyroclastic/spatter ramparts and **(b)** the lava channel with elevated rims. The black dashed lines show the mapped outlines of the rampart or lava deposits that allow us to determine the extent of the erupted material. The dashed lines perpendicular to the fissure and lava channel strike are the profile lines along which the CTX-based cross-sections were produced. Maps were produced using the Context Camera-based (CTX) digital elevation model (DEM) of stereo-pair images (P02_001774, centered at 4.86°N, 254.60°E, and B01_009949, centered at 4.46°N, 254.62°E). The corresponding cross-sections of the **(a')** volcanic fissure and **(b')** lava channel show the topography of the regions with the parameters determined in this study. The sides of the fissure and lava

channel are distinguished based on the map orientation towards the north. Both topographic profiles have vertical ticks every 5 m, making them equal in terms of scale. Abbreviations: the first letter indicates the direction (e.g., W – western side; E – eastern side), the second letter refers to the measured parameter (i.e., D – depth, T – thickness, etc.,) whereas the subscript depends on the feature (F – fissure and C – channel). The subscripts x of the thickness measurements indicate the distance of 50 meters between the points for which the measurements have been done.

4 Results and Interpretations

4.1 Geological mapping

To conduct a detailed investigation of the fissure vent-proximal deposits we mapped the volcanic landforms that are identifiable on the CTX images and corresponding 3D models (Fig. 3). Along the studied part of the fissure, we observed steep-sided accumulations of material that formed elevated rims, often on both sides (the upslope and downslope) of the vent (Fig. 3a-b). These elevated units are located within a narrow vent-proximal zone 100–200 m wide. They are characterized by a rough surface texture comprising short lobate-shaped structures. We interpret these steep-sided and elevated rims to be pyroclastic or spatter ramparts. Here, the term spatter is used as an all-encompassing term representing pieces of fragmented lava ejected during an explosive eruption and typically still hot and mobile. It is indeed likely that the pyroclastic constructs also contain large ballistic blocks, scoria, and fine ash in minor quantities, for example. The ramparts, in some parts, are interrupted by regions of lower rim elevation that constitute the breaks in the continuity of rampart deposits from which smooth-surface lava flows have spread (Fig. 3c). We observe that these flows have varying morphologies. On the western flank, these lava flows are short, up to 1 km in length, whereas on the opposite (i.e., eastern) flank, they merge forming larger flow units that migrated downslope, up to 7 km in length (Fig. 1c). This spatial distribution is likely controlled by the regional topography of the area, as on the western side, the elevation increases (i.e., overall upslope trend). This is caused by the presence of a volcanic center located to the northwest of the studied fissure (Fig. 1b) from which downslope-spreading lava flows have blocked the migration of lava from the studied fissure.

In addition to the latest volcanic products, on the western side of the fissure we identified older landforms that predate the formation of the vent-proximal deposits. This interpretation is supported by CTX image observations (Fig. 3) which allow us to define the boundaries of volcanic units by tracking grey-scale variations within the images, further supplemented by the DEMs and topographical cross-sections that reveal relative stratigraphic relationships between the identified units (Fig. 3). They form narrow channels that become wider with increasing distance from the fissure and as they are associated with the flow units, we interpreted them as outflow lava channels (Fig. 3c). However, their original extent is difficult to map, as they are partially covered by lava flows originating from the upslope-situated volcanic centers. Therefore, we assert that some of the fissure-associated landforms might be partially buried by the NW-originated lava flows characterized by the rough texture of their surfaces (Fig. 3c).

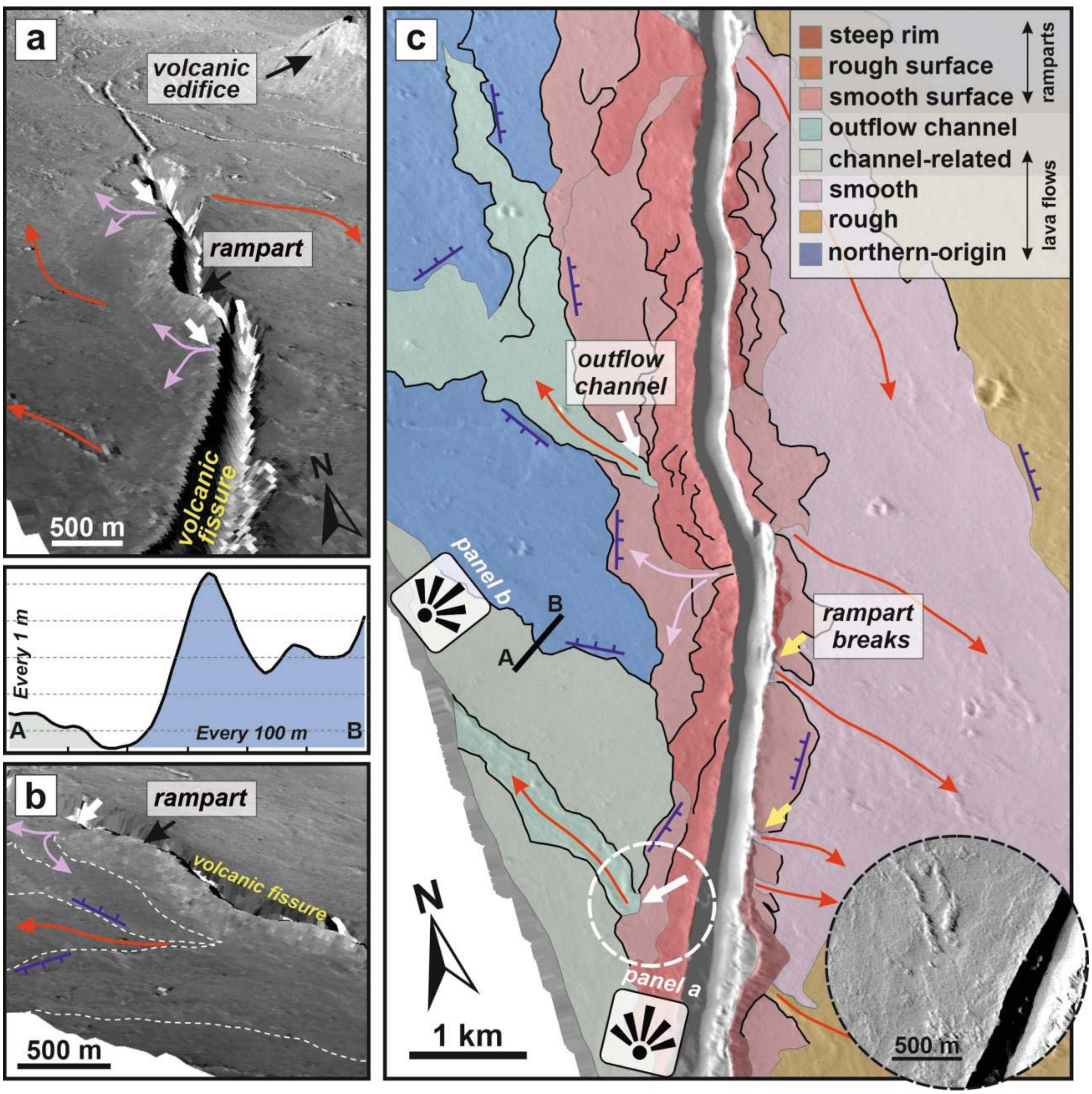

Fig. 3 High-resolution geological map of the volcanic fissure and spatter ramparts. **(a & b)** 3D visualizations of the volcanic fissure showing the generalized volcanology and the stratigraphic relationships between the individual lava flows indicating their relative age. The blue lines with hachures (ticks) on the side of overlying unit indicate the stratigraphically higher unit. These observations are supplemented by the corresponding cross-section (A-B) marked in panel c. The white arrows mark the location of outflow channels, whereas yellow the rampart breaks. The solid lines with arrows indicate the presumed direction of lava flows. Violet arrows are related to the smooth lava flows originating from the rampart material interpreted as rheomorphic flows. The red arrows are associated with topographic breaks in the rampart and thus are interpreted to be related to lava discharge from the vent. Produced using the CTX-based DEM of stereo-pair images (P02_001774, centered at 4.86°N, 254.60°E, and B01_009949, centered at 4.46°N, 254.62°E). These visualizations are vertically exaggerated 10 times. **(c)** A schematic geological map showing the mapped volcanic units associated with the fissure. Base map produced using CTX image P02_001774_1848. The solid black lines mark the vent-proximal deposits' outlines detected in the CTX images, whereas the solid grey lines constitute the outlines of the mapped units. The lower inset shows that the vent-proximal deposits buried the lava channel products.

The studied fissure system has a clear geological relationship to the elongated lava channel that propagates downslope from the vent to the east (Figs. 1c-d and 4a). The lava channel is sourced from an outflow originating at the fissure vent (Fig. 4b-c). This outflow point is well developed and unmodified. It shows a smaller anastomosing channel superimposed within the main channel. As shown in Figure 4c, the channel rims located close to the fissure are partially covered by lava originating from the fissure. Thus, to avoid misinterpretation of the structures formed by the overlapping of products, we omitted the first vent-proximal 2 km of the lava channel from any thickness/geomorphological observations. At downflow locations, where neither vent-proximal deposits nor post-channel formation productions co-exist, we found that the surfaces in contact with the channel are rough, consisting of blocks or accumulated lava fragments (Fig. 4d). They extend up to 300 meters from the channel rim. Furthermore, on both sides of the channel elevated rims are sometimes present. We interpret these to be associated with over-spilling lava flows and thus the formation of lava levees (Fig. 4). Along the strike of this channel, almost 7 km away from the fissure vent, the small lava channel spreads from the main lava channel (Fig. 4a-b and d). Our detailed structural mapping allows us to measure the morphological parameters and thickness of the deposits proximal to both the vent and channel.

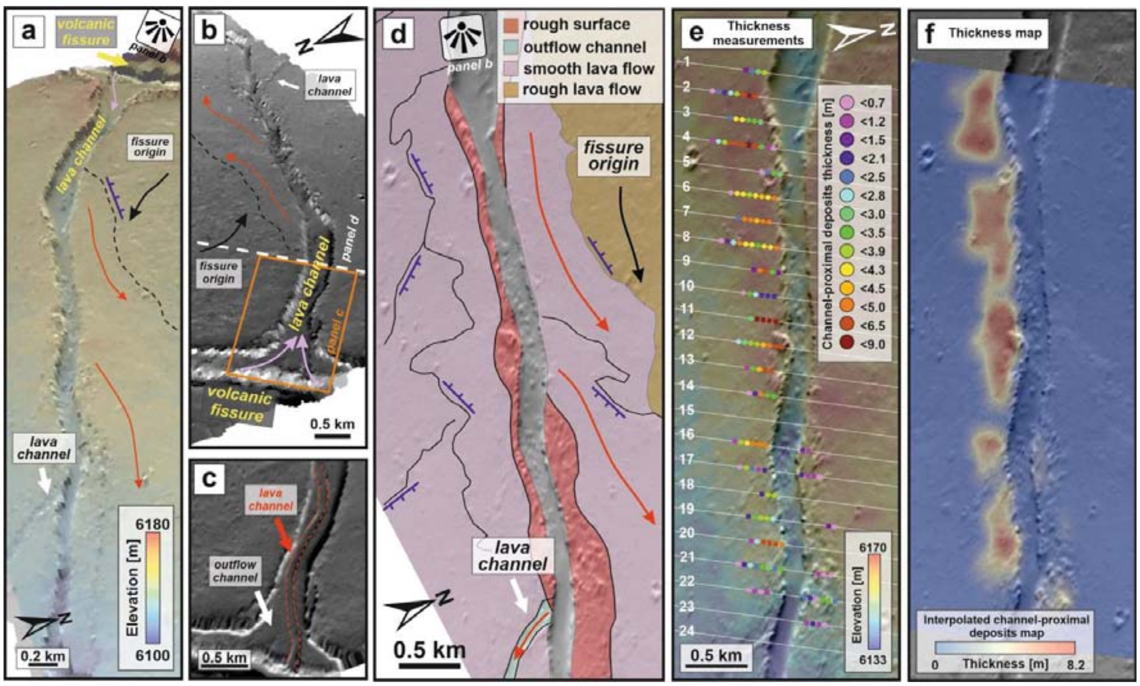

Fig. 4 High-resolution geological mapping of the lava channel and associated deposits. **(a & b)** An overview 3D visualization of the lava channel. The blue lines with hachures (ticks) are on the side of the overlying unit and therefore indicate the stratigraphically higher unit. The dashed black lines mark the location of inferred boundary between the lava units. Produced using the CTX-based DEM of stereo-pair images (P02_001774, centered at 4.86°N, 254.60°E, and B01_009949, centered at 4.46°N, 254.62°E). All visualizations are vertically exaggerated 10 times. **(c)** Close-up image of the vent-proximal part of the lava channel originating from the fissure (CTX image P02_001774_1848). **(d)** A schematic geological map presenting the different volcanic units associated with the studied lava channel. The base map is produced using CTX image P02_001774_1848. The solid black lines mark the lava flows outlines detected in the CTX images. **(e)** The channel-proximal deposits thickness measurements determined every 50 meters along the profile lines. For the methodology description, see the Method section. The basemap is a combination of a CTX image overlapped by a CTX-based DEM. **(f)** The channel-proximal deposits thickness map is produced by the interpolation tool in the ArcMap software applying the natural neighbor method.

4.2 Morphological characteristics of the fissure vent and ramparts

Using the detailed structural mapping, we produced 36 cross-sections approximately perpendicular to the fissure vent strike and measured the morphological parameters of both the fissure and associated spatter ramparts (Fig. 2a). We found that the fissure depth is highly variable and depends on the side of the fissure from which the measurement was performed. These discrepancies in the fissure depth are up to 16.5 meters between the rim sides (Fig. S3). In general, the fissure depth ranges from 16.4 to 58.2 m with an average value of ~33 ± 8 m (1 SD; standard deviation) (Table 1 and Fig. S3). The fissure width is also variable and ranges from 234 to 495 m. Notably, the width measured in one cross-section may vary up to 100 m depending on the measuring side of the fissure (see Fig. 2). The calculated average fissure width is 353 ± 48 m (1 SD). Combining the structural mapping and cross-sections, we found that the spatter deposits are heterogeneously distributed on both sides of the fissure vent. The spatial extent of the vent-proximal deposits on the western side ranges from 290 up to 1367 meters away from the fissure rim, whereas on the other side, the spatial extent is from 149 to 814 meters (Table 1). This discrepancy in the spatial distribution is also expressed by the thickness measurements of the spatter ramparts whose maximum values are 32 and 19 meters on the western and eastern side, respectively (Fig. 5a-b). A similar spatial trend is also shown by average values of maximum spatter rampart thickness of 17 ± 8 (western side) and 10 ± 4 meters (eastern side). By applying individual thickness measurements every 50 m along the profile lines, we were able to map the increase in the rampart thickness (Fig. 5c). The steepest rampart slopes with the highest increase of thickness occur close to the fissure rim with more gentle slopes further away from the fissure.

Table 1 Morphological characteristics of the studied volcanic fissure vent south of Ascraeus Mons. The graphical presentation of the methodology of measurements is shown in Figure 2.

No. of profile	Distance along fissure [m]	Depth [m]		Avg. depth [m]	SD [m]	Width [m]		Avg. width [m]	SD [m]	Rampart extent [m]		Max. apparent thickness of rampart deposits [m]	
		West	East			West	East			West	East	West	East
1	0	34.7	47.9	41.3	6.6	269.7	338.3	304.0	34.3	1212.9	177.4	10.9	4.8
2	200	41.7	58.2	49.9	8.3	310.5	368.0	339.3	28.7	1249.8	182.7	12.8	7.0
3	400	44.8	58.1	51.5	6.6	388.9	417.1	403.0	14.1	1276.9	318.3	18.2	7.1
4	600	37.5	49.6	43.5	6.1	329.1	384.0	356.6	27.4	1367.0	319.2	19.6	10.0
5	800	41.7	44.4	43.0	1.4	359.1	386.0	372.6	13.5	1335.3	272.2	28.8	8.0
6	1000	38.7	40.9	39.8	1.1	321.3	338.5	329.9	8.6	1049.8	404.6	28.3	12.4
7	1200	32.2	33.9	33.1	0.9	349.9	362.7	356.3	6.4	1349.8	382.7	31.9	16.1
8	1400	42.2	39.9	41.1	1.2	323.8	304.2	314.0	9.8	1279.8	247.2	32.1	13.2
9	1600	42.2	31.8	37.0	5.2	357.7	319.3	338.5	19.2	1249.8	286.2	27.1	9.4
10	1800	33.6	23.8	28.7	4.9	340.7	290.7	315.7	25.0	1199.8	398.3	28.5	13.9
11	2000	27.4	18.4	22.9	4.5	297.9	234.0	266.0	31.9	1186.3	462.9	25.7	15.9
12	2200	27.4	19.6	23.5	3.9	326.2	259.4	292.8	33.4	1199.8	610.7	22.4	18.5
13	2400	33.0	24.7	28.9	4.2	416.6	316.6	366.6	50.0	1069.8	399.9	21.4	13.0
14	2600	48.2	35.6	41.9	6.3	388.1	324.4	356.3	31.9	1223.1	381.4	22.5	10.5
15	2800	43.5	37.3	40.4	3.1	383.5	310.2	346.9	36.6	989.5	382.1	19.5	9.3
16	3000	32.9	28.8	30.9	2.1	392.8	332.3	362.5	30.3	899.9	399.9	18.8	9.2
17	3200	29.6	30.0	29.8	0.2	325.1	338.9	332.0	6.9	599.9	813.5	23.3	16.3
18	3400	32.6	34.3	33.4	0.8	314.6	336.7	325.6	11.0	532.5	724.7	21.0	12.8
19	3600	23.1	28.3	25.7	2.6	280.3	317.6	298.9	18.6	875.6	646.1	15.2	15.0
20	3800	33.3	31.7	32.5	0.8	325.4	296.3	310.8	14.6	773.5	466.4	16.4	13.7
21	4000	45.5	41.3	43.4	2.1	435.6	395.7	415.7	20.0	727.4	148.5	17.7	6.9
22	4200	53.2	42.9	48.1	5.2	413.9	344.3	379.1	34.8	1131.8	200.0	18.2	7.6
23	4400	50.2	42.9	46.6	3.6	354.5	315.0	334.8	19.8	862.5	256.8	14.6	7.8
24	4600	27.6	27.0	27.3	0.3	337.1	322.4	329.8	7.3	641.9	643.0	7.1	6.4
25	4800	27.7	24.7	26.2	1.5	334.2	315.6	324.9	9.3	599.9	399.9	7.2	4.4
26	5000	26.7	31.1	28.9	2.2	338.1	367.5	352.8	14.7	686.1	181.4	7.7	6.8
27	5200	32.5	34.9	33.7	1.2	395.0	422.4	408.7	13.7	676.8	380.3	10.5	10.5
28	5400	29.5	31.5	30.5	1.0	300.9	343.0	322.0	21.1	678.2	282.4	9.3	8.6
29	5600	23.9	22.1	23.0	0.9	435.1	366.5	400.8	34.3	639.9	270.5	11.4	9.6
30	5800	19.8	24.0	21.9	2.1	301.9	331.3	316.6	14.7	665.7	411.1	15.9	15.9
31	6000	16.4	25.0	20.7	4.3	255.5	305.4	280.5	25.0	566.7	566.7	13.9	13.9
32	6200	22.9	24.8	23.9	1.0	349.9	375.4	362.6	12.7	437.1	437.1	11.3	11.3
33	6400	26.3	28.5	27.4	1.1	402.6	445.7	424.2	21.5	363.2	340.5	8.7	8.7
34	6600	31.2	34.6	32.9	1.7	415.6	466.5	441.0	25.5	553.1	247.0	10.1	10.1
35	6800	28.2	32.5	30.3	2.1	422.4	463.6	443.0	20.6	387.1	415.1	8.6	8.6
36	7000	30.4	32.5	31.5	1.0	469.5	494.9	482.2	12.7	290.1	183.3	4.8	2.9

SD – standard deviation; avg. – average; max. – maximum.

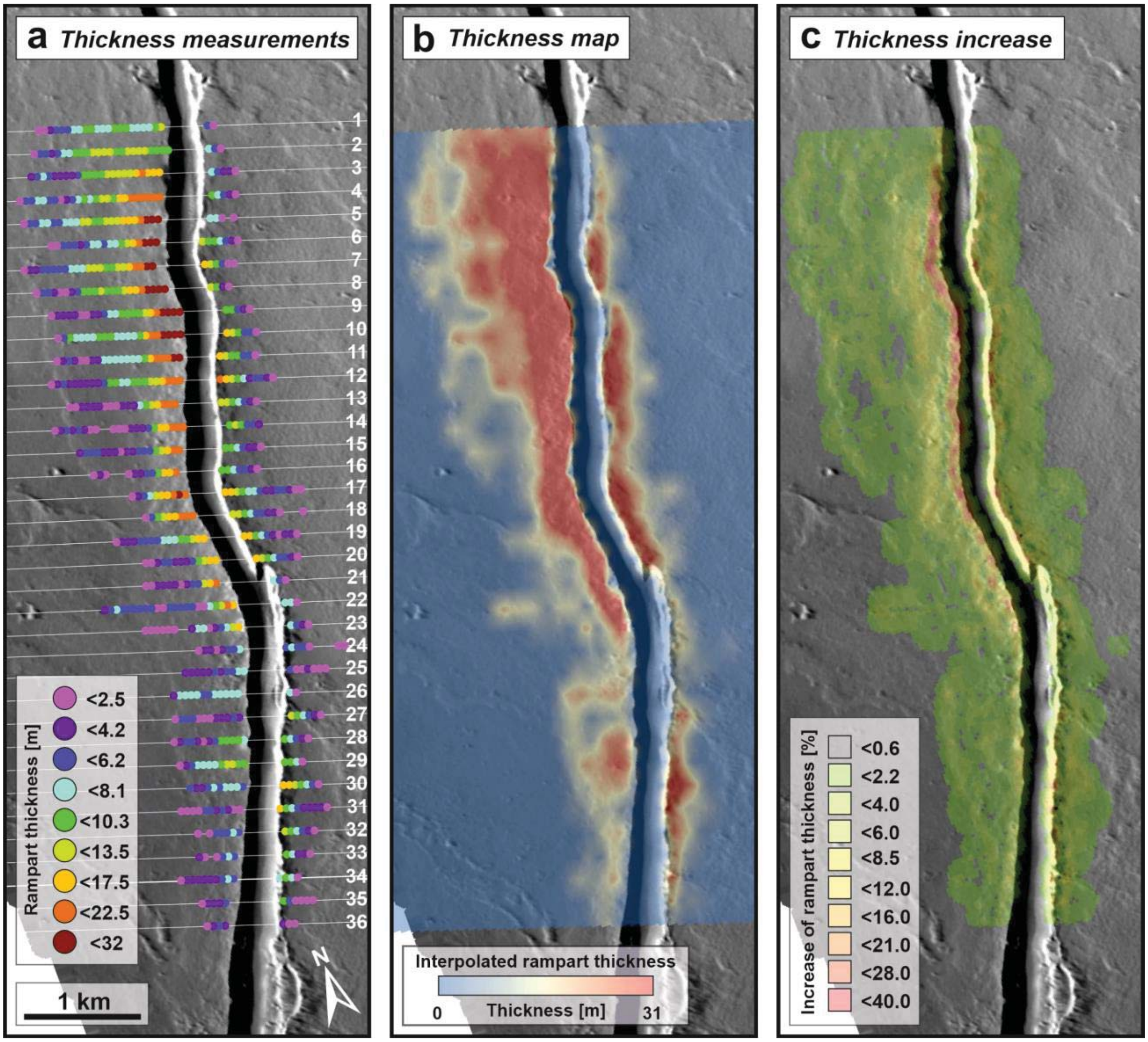

Fig. 5 Morphological characteristics of the spatter ramparts. **(a)** Rampart thickness data points collected every 50 meters along the (sequentially numbered) profile lines. The profiles are approximately perpendicular to the mid-plane along the fissure strike. Each coloured point represents an individual measurement of the rampart thickness based on our CTX-based cross-sections. **(b)** Interpolated rampart thickness map produced using the natural neighbour method. **(c)** A map presenting the increase in the rampart thickness (in percent rise) calculated based on the thickness measurements. The steepest ramparts occur close to the fissure rim with more gentle slopes further away from the fissure which agrees with our geological mapping.

4.3 Morphological characteristics of the lava channel

Based on the clear structural relationships between the studied fissure vent and the lava channel aligned downslope in the SE direction (Fig. 3a), we produced 24 cross-sections approximately perpendicular to the channel strike and, as for the fissure vent, we measured its morphological parameters (Table 2 and Fig. 4). We determined that the depth, along the channel length, is relatively homogeneous and ranges from 5.0 to 21.9 m with an average value of 13.0 ± 3.6 m (1 SD). The deepest part of the lava channel is located close to the fissure with an average depth of 19.7 ± 2.2 m (1 SD), with local lowering in its central part (up to 19.9 ± 1.0 m; 1SD), while the shallowest part is located distally with an average value of 6.6 ± 1.6 m (1 SD) (Fig. S3). Comparing the depth measurements on both sides of the channel, we found that the results obtained are very consistent with a low standard deviation (Table 2). The channel width decreases (average width from 519 to 275 m) with increasing distance away from the fissure (Table 2). Using our topographic profiles and geological mapping, we found that elevated channel-proximal deposits are mainly associated with its southern side whereas the opposite side is almost devoid of such elevated deposits (Fig. 4e-f). We measured the spatial extent of these deposits which range from 70 up to 593 m away from the channel with thicknesses up to 8.6 m (average value of 4.7 ± 1.6 m; Table 2 and Fig. 4e-f). As these channel-associated deposits are not so prominent as the fissure ramparts, we interpret them to be small volume overspills of lava originating from the channel. In addition, we found that these deposits occur mainly on the southern side of the channel, and therefore, we assert that their spatial distribution is controlled by the pre-eruption slope orientation (Fig. 4a-e).

Table 2 Morphological characteristics of the studied volcanic channel originating from the fissure vent south of Ascraeus Mons. The graphical presentation of the methodology of measurements is shown in Figure 2.

No. of profile	Distance along fissure [m]	Depth [m]		Avg. depth [m]	SD [m]	Width [m]		Avg. width [m]	SD [m]	Channel-proximal deposits extent [m]		Max. apparent thickness [m]	
		South	North			South	North			South	North	South	North
1	0	17.3	14.6	15.9	1.4	526.6	478.5	502.6	24.0	262.7	0.0	3.6	-
2	200	21.9	17.5	19.7	2.2	574.6	463.5	519.0	55.5	482.5	0.0	6.7	-
3	400	16.3	15.9	16.1	0.2	470.7	451.0	460.8	9.8	380.4	0.0	4.3	-
4	600	12.1	12.1	12.1	0.0	320.1	320.1	320.1	0.0	593.1	0.0	7.6	-
5	800	11.9	13.1	12.5	0.6	212.5	222.7	217.6	5.1	199.1	0.0	3.1	-
6	1000	12.2	10.5	11.3	0.9	298.7	270.8	284.7	14.0	393.8	0.0	4.8	-
7	1200	9.4	6.3	7.8	1.6	315.6	234.4	275.0	40.6	412.4	0.0	5.0	-
8	1400	13.3	13.3	13.3	0.0	298.3	298.3	298.3	0.0	547.8	0.0	4.9	-
9	1600	8.6	9.3	8.9	0.3	290.5	332.9	311.7	21.2	234.5	0.0	5.5	-
10	1800	12.7	15.6	14.1	1.5	264.7	324.1	294.4	29.7	326.5	0.0	3.3	-
11	2000	13.8	13.3	13.6	0.3	366.0	351.8	358.9	7.1	362.8	210.9	8.6	3.0
12	2200	13.5	10.4	11.9	1.5	314.8	242.4	278.6	36.2	532.2	78.7	5.4	0.9
13	2400	17.0	16.7	16.9	0.1	440.8	429.7	435.3	5.5	300.7	0.0	5.9	-
14	2600	11.9	18.6	15.3	3.4	256.0	294.6	275.3	19.3	275.9	0.0	4.5	-
15	2800	12.6	16.6	14.6	2.0	336.6	365.7	351.2	14.6	0.0	0.0	-	-
16	3000	18.9	21.0	19.9	1.0	285.7	310.1	297.9	12.2	296.7	69.7	4.9	1.4
17	3200	13.4	17.8	15.6	2.2	282.6	318.4	300.5	17.9	243.2	200.3	3.6	2.0
18	3400	10.2	6.5	8.3	1.9	328.2	261.3	294.8	33.5	209.5	0.0	3.6	-
19	3600	13.6	18.8	16.2	2.6	292.4	363.6	328.0	35.6	300.0	108.4	3.7	1.3
20	3800	14.3	12.4	13.3	1.0	326.7	281.0	303.9	22.8	333.9	0.0	6.0	-
21	4000	5.0	8.3	6.6	1.6	267.6	312.5	290.0	22.4	431.3	153.5	3.2	1.1
22	4200	6.3	8.8	7.6	1.3	231.8	250.0	240.9	9.1	212.5	268.1	0.9	3.4
23	4400	5.2	11.4	8.3	3.1	249.5	311.9	280.7	31.2	0.0	196.8	-	1.5
24	4600	8.9	13.1	11.0	2.1	236.4	274.1	255.2	18.9	0.0	0.0	-	-

SD – standard deviation; avg. – average; max. – maximum.

5 Discussion

5.1 Influence of data availability on detailed investigation of volcanic landforms

The Tharsis volcanic province hosts the largest areal coverage of the youngest (Late Amazonian) and best-preserved volcanic landforms on Mars (Hauber et al., 2011; Pieterek et al., 2022b; Richardson et al., 2021). This provides an unprecedented opportunity to conduct a detailed, high-resolution investigation of recent volcanic products. Eruptive vents are fundamental surficial features and their morphological parameters (length and width) for the entire Tharsis region have been determined by Richardson et al. (2021). However, although CTX and HiRISE images have been acquired for almost two decades (Keszthelyi et al., 2008; Malin et al., 2007), few studies have focused on the characterization and volcanological interpretation of vent-proximal deposits (Mouginis-Mark & Christensen, 2005; Wilson et al., 2009). This, in part, might be caused by the limited number of CTX-based DEMs which are crucial, as evidenced by this study, for structural mapping and quantitative morphological characterization. On Earth, in many cases, the formation of vent-proximal volcanic deposits (e.g., spatter cones, ramparts, vent agglutinate, lava ponds/lakes) can be monitored and supplemented with eye-witness accounts or constrained by sampling and petrological observations (e.g., Carracedo Sánchez et al., 2012; Jones et al., 2017, 2018; 2022a; 2022c; Orr et al., 2015; Parcheta et al., 2012, 2015; Rader et al., 2018; Reynolds et al., 2016; Sumner, 1998; Sumner et al., 2005). Such an approach is clearly not possible on Mars today, and therefore, here, we proposed a methodology to investigate small-scale, vent-proximal volcanic landforms associated with volcanic linear structures (Fig. 2). To date, the only known rampart geometries on Mars have been provided by Wilson et al. (2009) who determined the mean thickness of the vent-proximal deposits using MOLA-based topographical profiles. Although the vertical resolutions of both MOLA and CTX-based DEMs are comparable (1–2 meters; Guimpier et al., 2022; Mouginis-Mark et al., 2018), the MOLA spatial sampling is almost ~30 times coarser. Therefore the results obtained by Wilson et al. (2009) are less precise than what can now be achieved with CTX data. Thus, as more detailed topographical data become available, they provide increased opportunities to better characterize vent-proximal volcanic deposits.

The influence of the DEM spatial resolution on the obtained morphometry of small-scale volcanic landforms has been discussed by Brož et al. (2015). They showed that a CTX-based DEM provides a significant increase in accuracy in Martian topographic analysis relative to MOLA and HRSC DEMs. However, the most detailed topographic information can be obtained from the HiRISE DEMs (ground sampling distances and vertical resolution of < 1 m; Brož et al., 2015; Guimpier et al., 2022), but the Mars surface coverage of these data is low. The HiRISE imagery has currently covered ~0.5% of the surface of Mars with unique stereo-pair coverage. It therefore remains a challenge to systematically use HiRISE DEMs for vent-proximal processes. Here, by applying a CTX-based DEM in this study, we likely provide the currently most accurate morphological characterization of vent-proximal deposits on Mars. Among these deposits, in addition to the spatter ramparts, we also mapped the (clastogenic/rheomorphic) lava flows whose emplacement is likely to reflect the last stages of the eruption. In terrestrial studies, distinguishing between lava flows and spatter deposits is quite reliable. On Earth, field-based investigations can provide even millimeter-to-centimeter-scale observations (Jones et al., 2018; Rader et al., 2018). However, on Mars, our observations are limited to meter or even several meters scale. For example, we are unable to observe the interior textures of Martian lava flows to allow for a full assessment of a clastogenic/rheomorphic vs. purely effusive origin. Regarding the fissure-related products, it is therefore impossible to confidently distinguish between flows generated by lava overspills spreading from the vent vs. those reassembled from pieces of fragmented lava erupted in an explosive manner (e.g., rheomorphic lava flows). Although the mapping, and therefore the spatial characterization, of Martian vent-proximal deposits must be generalized and simplified (Fig. 2), the data obtained can still reveal new information. Lastly, one additional caveat that should be considered here is a pre-eruption surface (e.g., ground slope) that affects the distribution of the deposits and their measurements. On Earth, if pre-eruption DEMs are not available, reconstructing the pre-eruption ground slope requires a time-consuming field based approach such as mapping tree mold depths (e.g., Jones et al., 2017; Parcheta et al., 2012). On Mars these techniques are not possible and often a regional scale ground slope has to be assumed to represent the pre-eruption topography (Chevrel et al., 2013; Wilson et al., 2009; Wilson & Mouginis-mark, 2001). Therefore, comparing our results with terrestrial examples of spatter deposits, we must be aware of uncertainties attributed to the limitations of data availability.

5.2 Characteristics of vent-proximal deposits

On Earth, vent-proximal spatter ramparts are formed under a specific set of conditions that allows for quantitative prediction of cooling and accumulation rates (Head & Wilson, 1989; Rader et al., 2018; Rader & Geist, 2015; Sumner et al., 2005). Such constraints then provide insight into the eruption parameters that formed past deposits. For Mars, we still lack direct measurements of the spatter clasts, and therefore remote mapping provides a fundamental approach to understanding the eruptive environment. On Earth, for example, drone-based mapping supplemented by ground-truth was successfully used for investigating volcanic features such as lava flows (Favalli et al., 2018) and spatter rampart deposits (Sutton et al., 2024). For spatter ramparts to form, magma fragmentation is required (i.e., the breakage of magma into discrete pieces). These clasts of fragmented magma, termed here as spatter, must then be deposited relatively hot and mobile. If the amount and rate of cooling are too high, and clasts are deposited below their glass transition temperature, scoria deposits and cones will form.

Alternatively, if the amount and rate of cooling are low and the clast accumulation rate is sufficient, clastogenic or fountain-fed lavas will form.

On Earth, nearly all basaltic fissure eruptions have constructed spatter ramparts, for example, in Iceland (Eibl et al., 2017; Reynolds et al., 2016; Voigt et al., 2021; Witt et al., 2018), Italy (Branca et al., 2009; Mariotto et al., 2022), and the USA (Hughes et al., 2018; Valentine & Cortés, 2013). Ramparts are often produced from low (< 100 m) to moderate (100–400 m) Hawaiian-style lava fountains (Houghton et al., 2016, 2021; Jones et al., 2018; Parcheta et al., 2012, 2015; Richter et al., 1970; Witt et al., 2018). For instance, one of the youngest terrestrial spatter deposits was formed by the 2014–2015 Holuhraun fissure eruption (Iceland) that produced a steep-side (up to 45°; Sutton et al., 2024) vent-proximal edifice at the Baugur fissure vent (Voigt et al., 2021; Witt et al., 2018). Despite this widespread occurrence, to our knowledge, detailed quantitative geometrical descriptions of terrestrial spatter rampart deposits are only provided at one location (Parcheta et al., 2012, 2015, 2016). This previous field-based research focusing on the 1969–1974 Mauna Ulu eruption of Kīlauea provided an exceptional opportunity to study processes of low-intensity Hawaiian fissure fountaining and its associated volcanic landforms (Parcheta et al., 2012, 2015) and allows us to compare our Martian measurements with Earth data. Our documented Martian spatter rampart deposits are several times larger than those identified on Earth. For example, the spatter deposits attributed to the Mauna Ulu eruption reveal the thickness of the deposits ranging from 0.7 to 7.1 meters with a mean value of 4.4 meters. As in our study, the thickness variation was characterized along the fissure strike. The values of these variations are on the order of 1–2 m over a length scale of 2–3 m (Parcheta et al., 2012), whereas here, the applied methodology and spatial sampling of available data did not allow us to provide such detailed observations. On a larger scale, we also documented heterogeneity of the rampart's thickness which may indicate similar characteristics (Fig. S4). We interpret the total rampart thickness to be primarily controlled by a combination of the fountaining duration and the mass eruption rate. However, syn-eruptive processes such as rampart collapse and/or rafting by coeval lava flows may act to reduce rampart thicknesses and modify their lateral structures. Relative thickness variations along strike can be interpreted to represent along-strike variations in eruption intensity. Similar constraints have been provided for the 2014–2015 Holuhraun fissure eruption (Witt et al., 2018), where the relative high points likely record prolonged and/or more intense fountaining.

The most significant difference is in the spatial extent (width) of the spatter ramparts. The width of the Mauna Ulu spatter deposits range from 12 to 24 m (Parcheta et al., 2012) and the Baugur deposits from 30 to ~100 m (Sutton et al., 2024; Voigt et al., 2021), whereas the studied deposits on Mars are emplaced even up to ~1350 meters away from the fissure rim (Figs. 3 and 5). The greater extent of the mapped spatter deposits could be attributed to initial lava overspills, seepage of lava from underneath the ramparts, or rheomorphic flows that rafted the pyroclasts downslope. Nevertheless, these options are indistinguishable without ground-truth observations. Comparing general morphologies of ramparts on Earth and Mars, Wilson and Head (1994) pointed out that Martian spatter deposits might be slightly lower in height but the spatial extent should be broader. This is because the lower acceleration due to gravity, lower atmospheric pressure, and enhanced fragmentation rate on Mars will result in further transport of erupted pyroclasts (Brož et al., 2015; Wilson & Head, 1994). Moreover, such a large lateral extent of spatter deposits relative to terrestrial counterparts may be attributed to mapping limitations (preventing distinguishing a complex spatter rampart deposit's structure) or to our inclusion of rheomorphic flows that are able to flow much further away from the fissure vent rim than on Earth (Wilson & Head, 1994).

Despite the fact that the accumulation of fissure vent-proximal deposits interpreted as spatter ramparts has not been commonly identified on Mars (Keszthelyi et al., 2008; Mouginis-Mark & Christensen, 2005), which is in contradiction to the theoretical expectations (Wilson & Head, 1994), the current accessibility of high-resolution topographical data suggests that they may previously have been overlooked (Pieterek & Jones, 2023; Wilson et al., 2009).

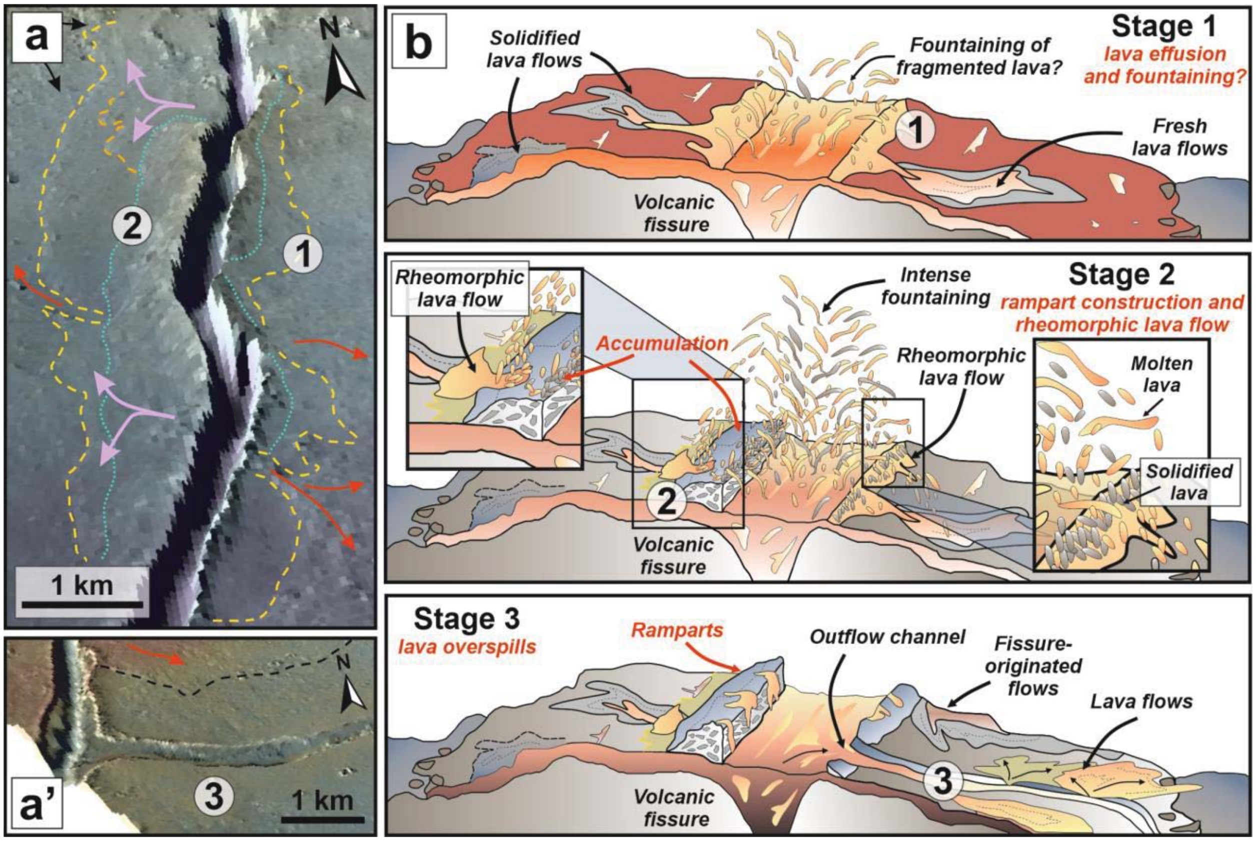

Fig. 6 Schematic reconstruction of rampart formation along Martian volcanic fissures. **(a)** 3D visualization of the volcanic fissure with schematic dashed and dotted lines showing the spatial extent of fissure-associated deposits. The yellow dashed lines refer to smooth units of the spatter rampart, whereas cyan dotted lines mark the extent of the rough surface of the spatter rampart deposits mapped (the reader is also referred to Figure 3). The solid lines with arrows indicate the presumed direction of lava flows. Violet arrows are related to the smooth lava flows originating from the rampart material interpreted as rheomorphic flows. The red arrows represent topographic breaks in the rampart and thus are interpreted to be related to lava discharge from the vent. The arrow colours are the same as in Figure 3. The lower panel (a’) displays the 3D view of the lava outflow channel originating from the volcanic fissure. The numbers correspond to panels on the right that present stages of the fissure evolution. These images were produced the same as in Figure 2. **(b)** Three stages of the evolution of the volcanic fissure and development of the associated spatter deposits (ramparts) formed by the accumulation (in Stage 2) of fragmented lava. For a detailed description, the reader is referred to the main text.

5.3 Eruption dynamics of fissure system

The studied spatter deposits associated with the fissure vent reveal an intriguing asymmetry (Fig 3). Such asymmetry partially contrasts with the only other Martian spatter rampart characterization, provided by Wilson et al. (2009), who evidenced similar rampart emplacement on both sides of the fissure. Here, the mapped spatter ramparts are also preserved on both sides of the fissure, but the geomorphological characteristics are different (e.g., height and spatial extent). This indicates that eruption-associated processes affected their appearance and geometry. On Earth, the asymmetric distribution of spatter deposits is mainly controlled by local syn-eruptive dynamics (e.g., rampart collapse, non-vertical feeder dike), wind, and ground slope. However, here the Martian fissure is located south of Ascraeus Mons where the regional elevation is > 5 km above the Martian datum, thus the effect of wind should have been negligible, which is supported by global wind patterns (Hayward et al., 2014). We therefore suggest that syn-eruptive dynamics and ground slope are the main controlling factors.

Although the mapped units are too small for absolute age determinations by crater counting, clear stratigraphic relationships between depositional units allow us to provide a spatiotemporal reconstruction of the eruptive sequence (Fig. 6). Thus, we can propose a simplified model of the last stages of the fissure eruption. Although most of the older deposits are completely or partially buried by younger landforms, the main phase of the eruption was likely due to the effusion of lava flows and potentially initial lava fountaining (Stage 1; see Fig. 6). These Stage 1 lavas extend ~2 km from the vent on the western flank, whereas, on the opposite flank, they merge forming flow units that migrated downslope for up to 7 km. The relatively large spatial extent covered by these Stage 1 flows indicates a relatively high lava effusion rate. It is impossible to determine whether Stage 1 was purely effusive or also included explosive activity that produced small pyroclastic ramparts/cones, that were destroyed by later eruptive stages.

Stratigraphically above the Stage 1 lavas lie the Stage 2 deposits that we directly associate with the spatter rampart. As detailed in Figure 3, these range in surface texture from smooth to rough, with the smoother surface deposits occurring at more vent-distal locations. The Stage 2 deposits (i.e., the pyroclastic ramparts) are emplaced on both sides of the fissure, extend between ~150 and ~1370 m from the fissure vent, and have irregular, lobate distal margins. The smooth-surfaced distal regions of these deposits were likely formed by rheomorphic flow following coalescence of hot pyroclasts erupted during periods of intense lava fountaining at the fissure vent. Spatter clasts were deposited hot, with a sufficient accumulation rate such that the material could behave rheomorphically and produce, at least in part, clastogenic or spatter-fed lava flows. The more vent-proximal, rougher surface deposits are interpreted to represent the more clastic end member of the spatter rampart deposits, with steeper deposit geometries and less to no rheomorphic flow. Some regions of the spatter rampart also display abrupt breaks in slope that are elongated approximately parallel to the fissure vent. We interpret these to be scarps or failure planes where the spatter rampart has (partly) collapsed (Le Moigne et al., 2020; Sumner, 1998; Sumner et al., 2005; Voigt et al., 2021) either syn- or post- eruption. In some cases, rampart failure was so widespread that an entire portion of the rampart failed and became the locus of lava effusion from the vent. There is clearly a continuum between these processes, and we expect clastic deposit formation, rheomorphic flow, deposit failure, and lava effusion from the vent to all occur repeatedly, probably simultaneously during a highly dynamic eruption environment. Like many mafic eruptions witnessed on Earth, this Martian eruption therefore straddled the effusive to explosive transition, simultaneously undergoing lava effusion and lava fragmentation (i.e., explosive behaviour) to form spatter clasts.

As evidenced by relics of spatter rampart deposits at the mouth of the channel spreading from the fissure vent (Fig. 4), towards the end of the eruptive sequence, the eastern side of the rampart experienced a large failure leading to the generation of a large (~575 m width close to the source vent) lava channel (Stage 3). This channel shows evidence for multiple, successive periods of lava effusions and outflow from the fissure vent (Fig. 4b-c). The channel margins feature a rough surface and a slightly elevated topography. We interpret these elevated rims (i.e., leeves) to form by successive lava overspills from the channel occurring when the lava effusion rate exceeded the volumetric capacity of the channel. Furthermore, as evidenced by our mapping and elevation data, the lava overspills preferentially occur on the southern slopes of the lava channel because the general topography of the region decreases in the SE direction (Fig. 4a). Lava propagating from the channel to the south was capable of migrating downslope whereas, on the other side, lava was blocked by the topography and the fissure-associated lava flows (Fig. 4d). Thus, the lava overspills might have partially drained-back into the channel.

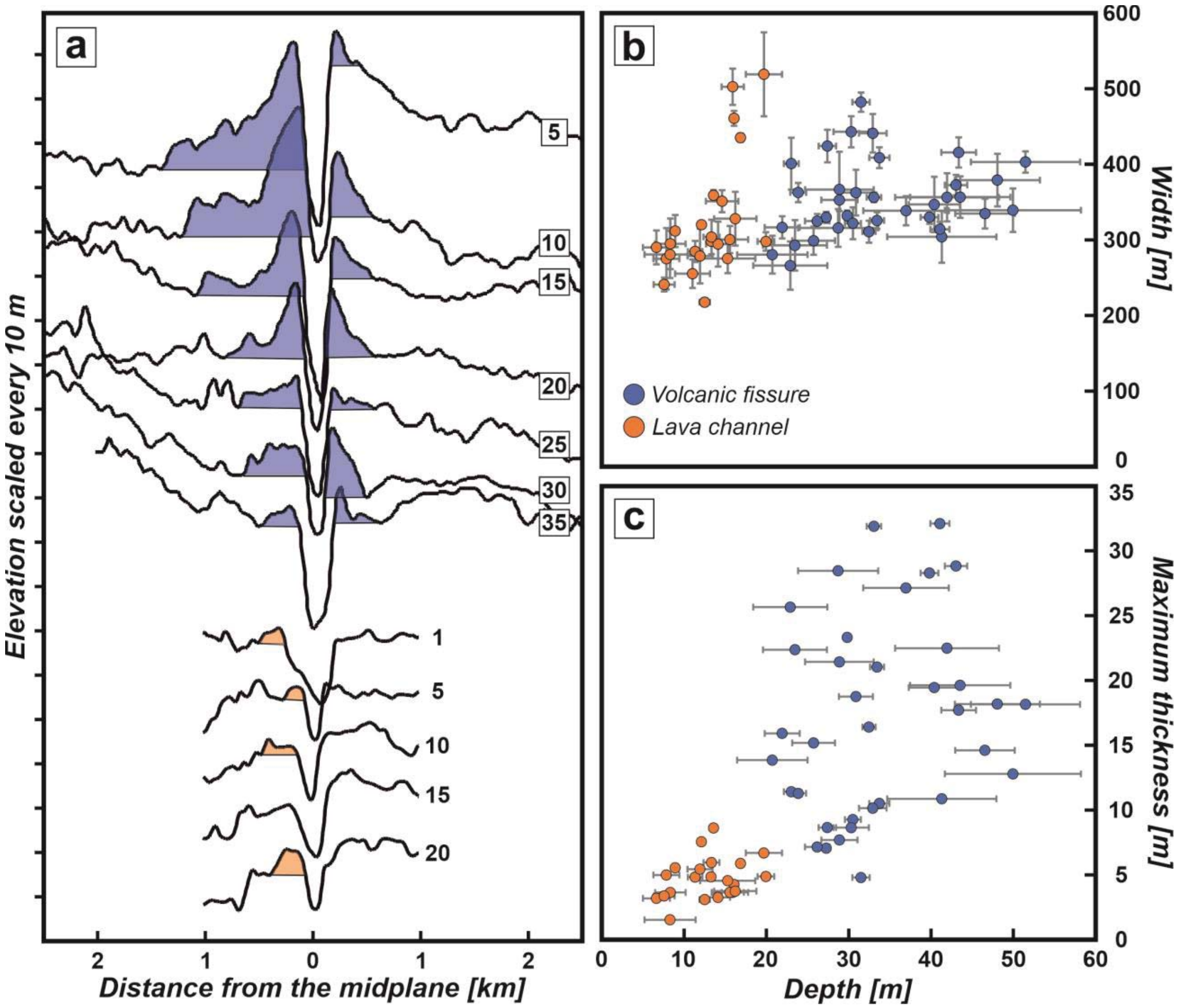

Fig. 7 Morphological comparison between the studied volcanic fissure and lava channel. **(a)** Selected cross-sections produced approximately perpendicular to the volcanic fissure and lava channel strikes using CTX-based DEM of stereo-pair images (P02_001774, centered at 4.86°N, 254.60°E, and B01_009949, centered at 4.46°N, 254.62°E). Cross-section numbers refer to the profile lines numbered in Figures 4 & 5. All cross-sections have the same scale, 10 m per tick mark. **(b)** The average depth vs. width measured and calculated on both sides of the investigated volcanic features. For detailed description refer to the Method section and Figure 2. The error bars represent 1 SD. **(c)** The average depth vs. maximum thickness (including both sides of the profiles) of the associated deposits.

5.4 Differentiation of spatter ramparts from other linear features

As the Martian surface has been predominantly shaped by volcanic activity, especially in the volcanic provinces, we can observe diverse volcanic features and landforms (Hauber et al., 2009; Wilson & Head, 1994). Notably, past fluvial and glacial erosional processes on Mars also created diverse linear features (Adeli et al., 2016; Baker et al., 2015; Conway et al., 2018;

Hubbard et al., 2014) that may share some similarities with volcanic-origin fissure vents or lava channels. Given the different generative processes, we may expect characteristic variations in their morphology. Therefore, detailed morphological descriptions of well documented, known volcanic features might provide important insights for further distinguishing linear features of debatable origin. For instance, within the Tharsis volcanic province, the southern lava aprons of the Tharsis Montes volcanoes are dominated by linear depressions and associated flow-like units (Bleacher et al., 2007). However, on the northern and western slopes of the Arsia Mons volcano, there is evidence of volcanism-induced melting of glaciers (Scanlon et al., 2014, 2015) which also involved the formation of linear features. This provides clear evidence that linear features of various origins can occur in close proximity to one another. In this study, to morphologically characterize volcanic linear features, we chose the particular region that is situated south of Ascraeus Mons as it constitutes a part of the Late Amazonian dike-fed volcanic field (Pieterek et al., 2022b; Richardson et al., 2021). This allows us to unambiguously identify differences between the studied linear structures comprising (i) the eruptive fissure vent and (ii) the lava channel. Even though the mapped features are of volcanic origin, they have been formed, by different volcanic processes.

We demonstrated that the width of both volcanic structures is within a similar range of values (234–494 vs. 213–575 meters for fissure and channel, respectively); however, the parameter that differs significantly is depth (Fig. 7). Using CTX-based cross-sections, we demonstrated that the fissure vent is almost two times deeper (16–53 meters) than the lava channel (5–22 meters). A similar fissure depth range (~20 to 58 meters) has been determined for the fissure vent to the east of the volcano Jovis Tholus (Mouginis-Mark & Christensen, 2005) that is accompanied by spatter rampart deposits investigated by Wilson et al. (2009). Also, Pieterek and Jones (2023) showed that the fissure system south of Pavonis Mons, with elevated rims interpreted as spatter ramparts, has vent depths ranging from ~30 up to as much as ~120 meters. These results indicate that, in general, fissure vents are typically deeper than lava channels (Fig. 7). Furthermore, the observed fissure depth is likely to be a minimum due to the drain back of lava during the waning eruption stages (Jones et al., 2017). Moreover, we found that the thickness of proximal deposits might also differentiate fissure vents from lava channels (Fig. 7c). As fissure vents are often the source of lava fountaining, they are commonly associated with pyroclastic/spatter ramparts. Such proximal rampart formation along fissure vents differs from proximal deposit formation at lava channels which is likely controlled by lava overspills that result in the formation of relatively low levees and small volume secondary lava flows.

6 Conclusions

Here, we presented high-resolution mapping of vent-proximal deposits coupled with CTX-based topographic data for a Martian fissure system. Our investigation has documented accumulations of pyroclastic deposits, likely spatter, along the fissure vent due to lava fountaining episodes representing eruptions on the very cusp of explosive activity. The clear spatial association between the fissure vent and a connected lava channel showed that the volcanic system experienced both explosive and effusive eruptions that occurred temporally close, and likely simultaneously. The preservation of both types of deposit allowed us to conduct a comparative analysis and reconstruct the late-stage eruption dynamics of the fissure system. We demonstrated that the spatial distribution of the spatter rampart deposits along the fissure vent is heterogeneous and likely caused by localization of more intense lava fountaining. On the other hand, channel-proximal deposits comprise levees produced by successive lava overspills whose emplacement was topographically controlled. Moreover, we found that the depth may constitute the parameter that best differentiates between these two volcanic structures (fissure vent vs. channel). These morphological characteristics can now be used to aid planetary mapping and the robust identification of linear features. Our observations indicate that although Amazonian-aged volcanism on Mars was predominantly controlled by effusive eruptions of low-viscosity magmas, the explosive-origin landforms, especially those formed by small volume, low-intensity eruptions, might have been overlooked in previous studies. Therefore, we suggest that additional studies are required to better understand the dynamic nature of Martian fissure eruptions and associated volatile release.

Data Availability Statement

The Mars Reconnaissance Orbiter Context Camera (CTX) images used for geological mapping in this study are freely available at the NASA Planetary Data System website (Malin, 2007). The global THEMIS-IR day time mosaic image is from Edwards et al. (2011) and the Mars Orbiter Laser Altimeter (MOLA) topographic data blended with the High Resolution Stereo Camera (HRSC) digital elevation model (DEM) used in this work are available in Fergason et al. (2018). The CTX-based DEM used for topographic measurements and 3D visualizations has been produced using MarsSI (Mars System of Information) – a system designed to process Martian orbital data (Quantin-Nataf et al., 2018). This system is available on the website https://marssi.univ-lyon1.fr. The produced DEMs is available at the MARSSI repository and in the Zenodo repository (Pieterek & Jones, 2024). The shapefiles containing the outlines of geological units, data pertaining to the thickness measurements of the spatter deposits, and Excel sheets that were used to prepare the figures, tables, and maps are available in the Zenodo repository (Pieterek & Jones, 2024).

Acknowledgments

We thank editor Bradley Thomson, Scott Hughes and an anonymous reviewer for their thorough and insightful comments that improved the manuscript. BP was supported by a Ministry of Education and Science (Poland) publication grant (62.9012.2401.00.0) and TJJ was supported by a UK Research and Innovation (UKRI) Future Leaders Fellowship (MR/W009781/1).

Author contributions

The project was conceived by B.P. and T.J. The data gathering and the production of graphics were completed by B.P. All authors contributed to the writing of the paper after an initial draft was prepared by B.P.

Competing interests

The authors declare that they have no known competing financial interests or personal relationships that could have appeared to influence the work reported in this paper.

References

Adeli, S., Hauber, E., Kleinhans, M., Le Deit, L., Platz, T., Fawdon, P., & Jaumann, R. (2016). Amazonian-aged fluvial system and associated ice-related features in Terra Cimmeria, Mars. *Icarus*, *277*, 286–299. https://doi.org/10.1016/j.icarus.2016.05.020

Apuani, T., Corazzato, C., Cancelli, A., & Tibaldi, A. (2005). Stability of a collapsing volcano (Stromboli, Italy): Limit equilibrium analysis and numerical modelling. *Journal of Volcanology and Geothermal Research*, *144*, 191–210. https://doi.org/10.1016/j.jvolgeores.2004.11.028

Baker, V. R., Hamilton, C. W., Burr, D. M., Gulick, V. C., Komatsu, G., Luo, W., et al. (2015). Fluvial geomorphology on Earth-like planetary surfaces: A review. *Geomorphology*, *245*, 149–182. https://doi.org/https://doi.org/10.1016/j.geomorph.2015.05.002

Bleacher, J. E., Greeley, R., Williams, D. A., Cave, S. R., & Neukum, G. (2007). Trends in effusive style at the Tharsis Montes, Mars, and implications for the development of the Tharsis province. *Journal of Geophysical Research: Planets*, *112*(9), 1–15. https://doi.org/10.1029/2006JE002873

Bleacher, J. E., Glaze, L. S., Greeley, R., Hauber, E., Baloga, S. M., Sakimoto, S. E. H., et al. (2009). Spatial and alignment analyses for a field of small volcanic vents south of Pavonis Mons and implications for the Tharsis province, Mars. *Journal of Volcanology and Geothermal Research*, *185*(1–2), 96–102. https://doi.org/10.1016/j.jvolgeores.2009.04.008

Branca, S., Del Carlo, P., Lo Castro, M. D., De Beni, E., & Wijbrans, J. (2009). The occurrence of Mt Barca flank eruption in the evolution of the NW periphery of Etna volcano (Italy). *Bulletin of Volcanology*, *71*(1), 79–94. https://doi.org/10.1007/s00445-008-0210-5

Brož, P., & Hauber, E. (2011). Windows of old fractured crust and associated volcanism in Tharsis, Mars. In *European Planetary Science Congress* (Vol. 6, p. EPSC-DPS2011-742-1). https://doi.org/10.1029/2011GL047310

Brož, P., & Hauber, E. (2012). A unique volcanic field in Tharsis, Mars: Pyroclastic cones as evidence for explosive eruptions. *Icarus*, *218*(1), 88–99. https://doi.org/10.1016/j.icarus.2011.11.030

Brož, P., Čadek, O., Hauber, E., & Rossi, A. P. (2015). Scoria cones on Mars: Detailed investigation of morphometry based on high-resolution digital elevation models. *J. Geophys. Res. Planets*, *120*, 1512–1527. https://doi.org/doi:10.1002/2015JE004873

Brož, P., Hauber, E., Wray, J. J., & Michael, G. (2017). Amazonian volcanism inside Valles Marineris on Mars. *Earth and Planetary Science Letters*, *473*, 122–130. https://doi.org/10.1016/j.epsl.2017.06.003

Brož, Petr, Čadek, O., Hauber, E., & Rossi, A. P. (2015). Scoria cones on Mars: Detailed investigation of morphometry based on high-resolution digital elevation models Petr. *Journal of Geophysical Research: Planets*, *120*, 1512–1527. https://doi.org/10.1002/2014JE004759.Received

Carr, M. H., & Head III, J. W. (2010). Geologic history of Mars. *Earth and Planetary Science Letters*, *294*(3–4), 185–203. https://doi.org/10.1016/j.epsl.2009.06.042

Carracedo Sánchez, M., Sarrionandia, F., Arostegui, J., Eguiluz, L., & Gil Ibarguchi, J. I. (2012). The transition of spatter to lava-like body in lava fountain deposits: Features and examples from the Cabezo Segura volcano (Calatrava, Spain). *Journal of Volcanology and Geothermal Research*, *227–228*(May), 1–14. https://doi.org/10.1016/j.jvolgeores.2012.02.016

Chevrel, M. O., Platz, T., Hauber, E., Baratoux, D., Lavallée, Y., & Dingwell, D. B. (2013). Lava flow rheology: A comparison of morphological and petrological methods. *Earth and Planetary Science Letters*, *384*, 109–120. https://doi.org/10.1016/j.epsl.2013.09.022

Conway, S. J., Butcher, F. E. G., de Haas, T., Deijns, A. A. J., Grindrod, P. M., & Davis, J. M. (2018). Glacial and gully erosion on Mars: A terrestrial perspective. *Geomorphology*, *318*, 26–57. https://doi.org/https://doi.org/10.1016/j.geomorph.2018.05.019

Edwards, C. S., Nowicki, K. J., Christensen, P. R., Hill, J., Gorelick, N., & Murray, K. (2011). Mosaicking of global planetary image datasets: 1. Techniques and data processing for Thermal Emission Imaging System (THEMIS) multi-spectral data. *Journal of Geophysical Research E: Planets*, *116*(10), 1–21. https://doi.org/10.1029/2010JE003755

Eibl, E. P. S., Bean, C. J., Jónsdóttir, I., Höskuldsson, A., Thordarson, T., Coppola, D., et al. (2017). Multiple coincident eruptive seismic tremor sources during the 2014–2015 eruption at Holuhraun, Iceland. *Journal of Geophysical Research: Solid Earth*, *122*(4), 2972–2987. https://doi.org/10.1002/2016JB013892

Favalli, M., Fornaciai, A., Nannipieri, L., Harris, A., Calvari, S., & Lormand, C. (2018). UAV-based remote sensing surveys of lava flow fields: a case study from Etna's 1974 channel-fed lava flows. *Bulletin of Volcanology*, *80*(3). https://doi.org/10.1007/s00445-018-1192-6

Fergason, R. L., Hare, T. M., & Laura, J. (2018). HRSC and MOLA Blended Digital Elevation Model at 200m v2. Retrieved from http://bit.ly/HRSC_MOLA_Blend_v0

Giacomini, L., Massironi, M., Martellato, E., Pasquarè, G., Frigeri, A., & Cremonese, G. (2009). Inflated flows on Daedalia Planum (Mars)? Clues from a comparative analysis with the Payen volcanic complex (Argentina). *Planetary and Space Science*, *57*(5–6), 556–570. https://doi.org/10.1016/j.pss.2008.12.001

Golombek, M. P., Grant, J. A., Crumpler, L. S., Greeley, R., Arvidson, R. E., Bell, J. F., et al. (2006). Erosion rates at the Mars Exploration Rover landing sites and long-term climate change on Mars. *Journal of Geophysical Research: Planets*, *111*(12), 1–14. https://doi.org/10.1029/2006JE002754

Guimpier, A., Conway, S. J., Pajola, M., Lucchetti, A., Simioni, E., Re, C., et al. (2022). Pre-landslide topographic reconstruction in Baetis Chaos, mars using a CaSSIS Digital Elevation Model. *Planetary and Space Science*, *218*(July 2021). https://doi.org/10.1016/j.pss.2022.105505

Hauber, E., Bleacher, J., Gwinner, K., Williams, D., & Greeley, R. (2009). The topography and morphology of low shields and associated landforms of plains volcanism in the Tharsis region of Mars. *Journal of Volcanology and Geothermal Research*, *185*(1–2), 69–95. https://doi.org/10.1016/j.jvolgeores.2009.04.015

Hauber, E., Brož, P., Jagert, F., Jodowski, P., & Platz, T. (2011). Very recent and wide-spread basaltic volcanism on Mars. *Geophysical Research Letters*, *38*(10), 1–5. https://doi.org/10.1029/2011GL047310

Hayward, R. K., Fenton, L. K., & Titus, T. N. (2014). Mars Global Digital Dune Database (MGD3): Global dune distribution and wind pattern observations. *Icarus*, *230*, 38–46. https://doi.org/10.1016/j.icarus.2013.04.011

Head, J. W., & Wilson, L. (1989). Basaltic pyroclastic eruptions: Influence of gas-release patterns and volume fluxes on fountain structure, and the formation of cinder cones, spatter cones, rootless flows, lava ponds and lava flows. *Journal of Volcanology and Geothermal Research*, *37*(3–4), 261–271. https://doi.org/10.1016/0377-0273(89)90083-8

Horvath, D. G., Moitra, P., Hamilton, C. W., Craddock, R. A., & Andrews-Hanna, J. C. (2021). Evidence for geologically recent explosive volcanism in Elysium. *Icarus*, *365*, 114499. https://doi.org/10.1016/j.icarus.2021.114499

Houghton, B. F., & Gonnermann, H. M. (2008). Basaltic explosive volcanism: Constraints from deposits and models. *Geochemistry*, *68*(2), 117–140. https://doi.org/https://doi.org/10.1016/j.chemer.2008.04.002

Houghton, B. F., Taddeucci, J., Andronico, D., Gonnermann, H. M., Pistolesi, M., Patrick, M. R., et al. (2016). Stronger or longer: Discriminating between Hawaiian and Strombolian eruption styles. *Geology*, *44*(2), 163–166. https://doi.org/10.1130/G37423.1

Houghton, B. F., Tisdale, C. M., Llewellin, E. W., Taddeucci, J., Orr, T. R., Walker, B. H., & Patrick, M. R. (2021). The Birth of a Hawaiian Fissure Eruption. *Journal of Geophysical Research: Solid Earth*, *126*(1), 1–17. https://doi.org/10.1029/2020JB020903

Hubbard, B., Souness, C., & Brough, S. (2014). Glacier-like forms on Mars. *Cryosphere*, *8*(6), 2047–2061. https://doi.org/10.5194/tc-8-2047-2014

Hughes, S. S., Kobs Nawotniak, S. E., Sears, D. W. G., Borg, C., Garry, W. B., Christiansen, E. H., et al. (2018). Phreatic explosions during basaltic fissure eruptions: Kings Bowl lava field, Snake River Plain, USA. *Journal of Volcanology and Geothermal Research*, *351*, 89–104. https://doi.org/10.1016/j.jvolgeores.2018.01.001

Jones, T. J., Llewellin, E. W., Houghton, B. F., Brown, R. J., & Vye-Brown, C. (2017). Proximal lava drainage controls on basaltic fissure eruption dynamics. *Bulletin of Volcanology*, *79*(11), 1–15. https://doi.org/10.1007/s00445-017-1164-2

Jones, T. J., Houghton, B. F., Llewellin, E. W., Parcheta, C. E., & Höltgen, L. (2018). Spatter matters-distinguishing primary (eruptive) and secondary (non-eruptive) spatter deposits. *Scientific Reports*, *8*(1), 1–12. https://doi.org/10.1038/s41598-018-27065-1

Jones, T. J., Reynolds, C. D., & Boothroyd, S. C. (2019). Fluid dynamic induced break-up during volcanic eruptions. *Nature Communications*, *10*(1), 1–7. https://doi.org/10.1038/s41467-019-11750-4

Jones, T. J., Le Moigne, Y., Russell, J. K., Williams-Jones, G., Giordano, D., & Dingwell, D. B. (2022a).

Inflated pyroclasts in proximal fallout deposits reveal abrupt transitions in eruption behaviour. *Nature Communications*, *13*(1), 2832. https://doi.org/10.1038/s41467-022-30501-6

Jones, T. J., Cashman, K. V., Liu, E. J., Rust, A. C., & Scheu, B. (2022b). Magma fragmentation: a perspective on emerging topics and future directions. *Bulletin of Volcanology*, *84*(5). https://doi.org/10.1007/s00445-022-01555-7

Jones, T. J., Russell, J. K., Brown, R. J., & Hollendonner, L. (2022c). Melt stripping and agglutination of pyroclasts during the explosive eruption of low viscosity magmas. *Nature Communications*, *13*(1), 992. https://doi.org/10.1038/s41467-022-28633-w

Keszthelyi, L., Jaeger, W., McEwen, A., Tornabene, L., Beyer, R. A., Dundas, C., & Milazzo, M. (2008). High resolution imaging science experiment (HiRISE) images of volcanic terrains from the first 6 months of the Mars reconnaissance orbiter primary science phase. *Journal of Geophysical Research: Planets*, *113*(4), E04005. https://doi.org/10.1029/2007JE002968

Malin, M. C. (2007). MRO context camera experiment data record level 0 V1.0 [dataset]. *NASA Planetary Data System*. https://doi.org/10.17189/1520266

Malin, M. C., Bell, J. F., Cantor, B. A., Caplinger, M. A., Calvin, W. M., Clancy, R. T., et al. (2007). Context Camera Investigation on board the Mars Reconnaissance Orbiter. *Journal of Geophysical Research: Planets*, *112*(5), E05S04. https://doi.org/10.1029/2006JE002808

Mariotto, P. F., Bonali, F. L., Tibaldi, A., De Beni, E., Corti, N., Russo, E., et al. (2022). A NewWay to Explore Volcanic Areas: QR-Code-Based Virtual Geotrail at Mt. Etna Volcano, Italy. *Land*, *11*(3), 377. https://doi.org/doi.org/10.3390/land11030377

Le Moigne, Y., Williams-Jones, G., Russell, K., & Quane, S. (2020). Physical volcanology of Tseax Volcano, British Columbia, Canada. *Journal of Maps*, *16*(2), 363–375. https://doi.org/10.1080/17445647.2020.1758809

Le Moigne, Y., Williams-Jones, G., Vigouroux, N., & Russell, J. K. (2022). Chronology and Eruption Dynamics of the Historic∼1700 CE Eruption of Tseax Volcano, British Columbia, Canada. *Frontiers in Earth Science*, *10*(June), 1–20. https://doi.org/10.3389/feart.2022.910451

Mouginis-Mark, P. J., & Christensen, P. R. (2005). New observations of volcanic features on Mars from the THEMIS instrument. *Journal of Geophysical Research*, *110*(8), 1–17. https://doi.org/10.1029/2005JE002421

Mouginis-Mark, P. J., Boyce, J., Sharpton, V. L., & Garbeil, H. (2018). Determination of Mars crater geometric data: Insights from high-resolution digital elevation models. *Meteoritics and Planetary Science*, *53*(4), 726–740.

Mouginis-Mark, P. J., Zimbelman, J. R., Crown, D. A., Wilson, L., & Gregg, T. K. P. (2022). Martian volcanism: Current state of knowledge and known unknowns. *Geochemistry*, *82*(4), 125886. https://doi.org/10.1016/j.chemer.2022.125886

Orr, T. R., Poland, M. P., Patrick, M. R., Thelen, W. A., Sutton, A. J., Elias, T., et al. (2015). Kilauea's 5-9 March 2011 Kamoamoa Fissure Eruption and Its Relation to 30+ Years of Activity From Pu'u 'ō 'ō. *Hawaiian Volcanoes: From Source to Surface*, (March 2011), 393–420. https://doi.org/10.1002/9781118872079.ch18

Parcheta, C. E., Houghton, B. F., & Swanson, D. A. (2012). Hawaiian fissure fountains 1: Decoding deposits-episode 1 of the 1969-1974 Mauna Ulu eruption. *Bulletin of Volcanology*, *74*(7), 1729–1743. https://doi.org/10.1007/s00445-012-0621-1

Parcheta, C. E., Fagents, S., Swanson, D. A., Houghton, B. F., & Eriksen, T. (2015). Hawaiian Fissure Fountains. In R. Carey, V. Cayol, M. Poland, & D. Weis (Eds.), *Hawaiian Volcanoes: From Source* *to Surface*. https://doi.org/10.1002/9781118872079.ch17

Parcheta, C. E., Pavlov, C. A., Wiltsie, N., Carpenter, K. C., Nash, J., Parness, A., & Mitchell, K. L. (2016). A robotic approach to mapping post-eruptive volcanic fissure conduits. *Journal of Volcanology and Geothermal Research*, *320*, 19–28. https://doi.org/10.1016/j.jvolgeores.2016.03.006

Peters, S. I., Christensen, P. R., & Clarke, A. B. (2021). Lava Flow Eruption Conditions in the Tharsis Volcanic Province on Mars. *Journal of Geophysical Research: Planets*, *126*(7). https://doi.org/10.1029/2020JE006791

Pieterek, B., & Jones, T. J. (2023). The evolution of Martian fissure eruptions and their plumbing systems. *Earth and Planetary Science Letters*, *621*, 118382. https://doi.org/10.1016/j.epsl.2023.118382

Pieterek, B., & Jones, T. J. (2024). Vent-Proximal Deposits South of Ascraeus Mons, Mars. Zenodo. https://doi.org/10.5281/zenodo.10263327

Pieterek, B., Laban, M., Ciążela, J., & Muszyński, A. (2022a). Explosive volcanism in Noctis Fossae on Mars. *Icarus*, *375*, 114851. https://doi.org/doi.org/10.1016/j.icarus.2021.114851

Pieterek, B., Ciazela, J., Lagain, A., & Ciazela, M. (2022b). Late Amazonian dike-fed distributed volcanism in the Tharsis volcanic province on Mars. *Icarus*, *386*, 115151. https://doi.org/10.1016/j.icarus.2022.115151

Pieterek, B., Brož, P., Hauber, E., & Stephan, K. (2024). Insight from the Noachian-aged fractured crust to the volcanic evolution of Mars: A case study from the Thaumasia graben and Claritas Fossae, *407*(July 2023), 115770. https://doi.org/10.1016/j.icarus.2023.115770

Quantin-Nataf, C., Lozac, L., Thollot, P., Loizeau, D., Bultel, B., Fernando, J., et al. (2018). MarsSI: Martian surface data processing information system. *Planetary and Space Science*, *150*(September 2017), 157–170. https://doi.org/10.1016/j.pss.2017.09.014

Rader, E., & Geist, D. (2015). Eruption conditions of spatter deposits. *Journal of Volcanology and Geothermal Research*, *304*, 287–293. https://doi.org/10.1016/j.jvolgeores.2015.09.011

Rader, E., Kobs Nawotniak, S., & Heldmann, J. (2018). Variability of Spatter Morphology in Pyroclastic Deposits in Southern Idaho, as Correlated to Thermal Conditions and Eruptive Environment. *Earth and Space Science*, *5*(10), 592–603. https://doi.org/10.1029/2018EA000377

Reynolds, P., Brown, R. J., Thordarson, T., & Llewellin, E. W. (2016). The architecture and shallow conduits of Laki-type pyroclastic cones: insights into a basaltic fissure eruption. *Bulletin of Volcanology*, *78*(5). https://doi.org/10.1007/s00445-016-1029-0

Richardson, J. A., Bleacher, J. E., Connor, C. B., & Glaze, L. S. (2021). Small Volcanic Vents of the Tharsis Volcanic Province, Mars. *Journal of Geophysical Research: Planets*, *126*(2), e2020JE006620. https://doi.org/10.1029/2020JE006620

Richter, D. H., Eaton, J. P., Murata, K. J., Ault, W. U., & Krivoy, H. L. (1970). Chronological narrative of the 1959-60 eruption of Kilauea Volcano, Hawaii. *Professional Paper. US Geological Survey*. https://doi.org/10.3133/pp537E

Robbins, S. J., Di Achille, G., & Hynek, B. M. (2011). The volcanic history of Mars: High-resolution crater-based studies of the calderas of 20 volcanoes. *Icarus*, *211*(2), 1179–1203. https://doi.org/10.1016/j.icarus.2010.11.012

Romero, J. E., Burton, M., Cáceres, F., Taddeucci, J., Civico, R., Ricci, T., et al. (2022). The initial phase of the 2021 Cumbre Vieja ridge eruption (Canary Islands): Products and dynamics controlling edifice growth and collapse. *Journal of Volcanology and Geothermal Research*, *431*(April).

https://doi.org/10.1016/j.jvolgeores.2022.107642

Scanlon, K. E., Head, J. W., Wilson, L., & Marchant, D. R. (2014). Volcano-ice interactions in the Arsia Mons tropical mountain glacier deposits. *Icarus*, *237*, 315–339. https://doi.org/10.1016/j.icarus.2014.04.024

Scanlon, K. E., Head, J. W., & Marchant, D. R. (2015). Volcanism-induced, local wet-based glacial conditions recorded in the Late Amazonian Arsia Mons tropical mountain glacier deposits. *Icarus*, *250*, 18–31. https://doi.org/10.1016/j.icarus.2014.11.016

Sibson, R. (1981). A brief description of natural neighbour interpolation. *Interpreting Multivariate Data*, 21–36.

Sumner, J. M. (1998). Formation of clastogenic lava flows during fissure eruption and scoria collapse: the 1986 eruption of Izu-Oshima Volcano, eastern Japan. *Bull Volcanol*, *60*, 195–212.

Sumner, J. M., Blake, S., Matela, R. J., & Wolff, J. A. (2005). Spatter. *Journal of Volcanology and Geothermal Research*, *142*(1-2 SPEC. ISS.), 49–65. https://doi.org/10.1016/j.jvolgeores.2004.10.013

Sutton, S. S., Richardson, J. A., Whelley, P. L., Scheidt, S. P., & Hamilton, C. W. (2024). Degradation of the 2014 – 2015 Holuhraun vent- proximal edi ce in Iceland Degradation of the 2014 – 2015 Holuhraun vent-proximal. *Bulletin of Volcanology*, *86*, 37. https://doi.org/10.1007/s00445-024-01709-9

Taddeucci, J., Edmonds, M., Houghton, B., James, M. R., & Vergniolle, S. (2015). Chapter 27 - Hawaiian and Strombolian Eruptions. In H. B. T.-T. E. of V. (Second E. Sigurdsson (Ed.) (pp. 485–503). Amsterdam: Academic Press. https://doi.org/https://doi.org/10.1016/B978-0-12-385938-9.00027-4

Valentine, G. A., & Cortés, J. A. (2013). Time and space variations in magmatic and phreatomagmatic eruptive processes at Easy Chair (Lunar Crater Volcanic Field, Nevada, USA). *Bulletin of Volcanology*, *75*(9), 1–13. https://doi.org/10.1007/s00445-013-0752-z

Vaucher, J., Baratoux, D., Toplis, M. J., Pinet, P., Mangold, N., & Kurita, K. (2009). The morphologies of volcanic landforms at Central Elysium Planitia: Evidence for recent and fluid lavas on Mars. *Icarus*, *200*(1), 39–51. https://doi.org/10.1016/j.icarus.2008.11.005

Voigt, J. R. C., Hamilton, C. W., Scheidt, S. P., Münzer, U., Höskuldsson, Á., Jónsdottir, I., & Thordarson, T. (2021). Geomorphological characterization of the 2014–2015 Holuhraun lava flow-field in Iceland. *Journal of Volcanology and Geothermal Research*, *419*. https://doi.org/10.1016/j.jvolgeores.2021.107278

Volat, M., Quantin-Nataf, C., & Dehecq, A. (2022). Digital elevation model workflow improvements for the MarsSI platform and resulting orthorectified mosaic of Oxia Planum, the landing site of the ExoMars 2022 rover. *Planetary and Space Science*, *222*, 105552. https://doi.org/https://doi.org/10.1016/j.pss.2022.105552

Vörös, F., & Székely, B. (2022). High-resolution DTM-based estimation of geomorphometric parameters of selected putative Martian scoria cones. *Icarus*, *377*. https://doi.org/10.1016/j.icarus.2022.114923

Werner, S. C. (2009). The global martian volcanic evolutionary history. *Icarus*, *201*(1), 44–68. https://doi.org/10.1016/j.icarus.2008.12.019

Wilson, L., & Head, J. W. (1994). Mars: Review and analysis of volcanic erupiton theory and relationships to observed landforms. *Reviews of Geophysics*, *32*(3), 221–263. https://doi.org/10.1029/94RG01113

Wilson, L., & Mouginis-mark, P. J. (2001). Estimation of volcanic eruption conditions for a large flank event on Elysium Mons, Mars. *Journal of Geophysical Research*, *106*(E9), 20621–20628.

Wilson, L., Mouginis-Mark, P. J., Tyson, S., Mackown, J., & Garbeil, H. (2009). Fissure eruptions in Tharsis, Mars: Implications for eruption conditions and magma sources. *Journal of Volcanology and Geothermal Research*, *185*(1–2), 28–46. https://doi.org/10.1016/j.jvolgeores.2009.03.006

Witt, T., Walter, T. R., Müller, D., Guðmundsson, M. T., & Schöpa, A. (2018). The Relationship Between Lava Fountaining and Vent Morphology for the 2014–2015 Holuhraun Eruption, Iceland, Analyzed by Video Monitoring and Topographic Mapping. *Frontiers in Earth Science*, *6*(December). https://doi.org/10.3389/feart.2018.00235

Zimbelman, J. R., Garry, W. B., Bleacher, J. E., & Crown, D. A. (2015). Volcanism on Mars. In I. A. Sigurdsson, B. Houghton, S. R. McNutt, H. Rymer, & J. Stix (Eds.), *The Encyclopedia of Volcanoes* (pp. 717–729). Elsevier.